NATIONAL ADVISORY COMMITTEE FOR AERONAUTICS

TECHNICAL NOTE 3680

INTERACTION OF GRIDS WITH TRAVELING SHOCK WAVES

By Darshan Singh Dosanjh

Johns Hopkins University

Corrected Copy

Washington
September 1956

NATIONAL ADVISORY COMMITTEE FOR AERONAUTICS

TECHNICAL NOTE 3680

INTERACTION OF GRIDS WITH TRAVELING SHOCK WAVES

By Darshan Singh Dosanjh

SUMMARY

Grids were mounted in the path of traveling shock waves in a shock tube. The incident shock wave after its collision with the grid split into transmitted and reflected shock waves. The emergence and the growth as well as the speeds of these shock fronts were recorded with shadowgraphic as well as with hot-wire techniques. It was observed that the distorted shock fronts emerging out of the grid became essentially normal and plane within an equivalent distance of about 12 mesh lengths.

When relatively strong incident shock waves were used, the grid choked. A simplified semiempirical analysis led to the conclusion that concurrent with this choking phenomenon the upstream flow approaching the grid assumed a constant Mach number. The calculated pressure-drop coefficient also exhibited the effect of the choking of the grid.

The reflected shock wave advances upstream against the drift flow associated with the incident shock wave. The flow behind the reflected shock front, however, is directed toward the grid. After its passage through the grid, the flow becomes turbulent. The transmitted shock front is reflected from the closed far end of the shock tube. The shadowgraphs of the interaction of the advancing reflected transmitted shock front with this turbulent flow field are examined and the observed change in the speed of the reflected-transmitted shock is discussed.

The oscillograms of the hot-wire response of various transient flow regions are examined and some preliminary conclusions regarding the state of the flow downstream of the grid are reached. Also a few suggestions for the extension of this work are included.

INTRODUCTION

The hot-wire anemometer is extensively used in turbulence research both in subsonic and in supersonic flows. In wind tunnels meant for turbulence research some fluctuations are usually purposely superimposed on the mean flow and the hot-wire anemometer is used to investigate the characteristics of these fluctuations.

Since the hot-wire anemometer has a comparatively fast response to fluctuations in flow conditions and/or in heating current, it has been successfully used to investigate transient flow phenomena in a shock tube (refs. 1 and 2).

The transient wave fronts and the associated mean flows may have in them some fluctuations inherently present or purposely introduced. The usual optical techniques (shadowgraph, schlieren, and interferometer) furnish only a limited amount of quantitative appraisal of such fluctuations in the transient flow fields (refs. 3 and 4). The hot-wire anemometer can also be usefully employed for such investigations.

It is hard to find a convenient and simple source of turbulence which can be adapted for investigations (such as shock-wave turbulence interaction) in a conventional shock tube. Some preliminary observations were made for the following cases.

In the theoretical analysis of the shock-tube flows the contact surface, that is, the boundary between the gas expanded from the compression chamber and the gas compressed from the expansion chamber, is normally assumed to be a sharp discontinuity across which there is a sudden change in temperature and density. The flow behind this surface is also assumed to be smooth. However, it is qualitatively known from optical observations (refs. 5 and 6) and has been confirmed by hot-wire investigations (refs. 2 and 7) that this surface is not a sharply defined thermodynamic discontinuity and that the flow behind this surface is highly turbulent. The intense turbulent fluctuations in this flow are caused by the rupturing characteristics of the ordinary cellophane sheets, the usual diaphragm material. The intensity and the character of these fluctuations are not precisely controllable. Thus, although the contact surface flow is intensely turbulent, its doubtful reproducibility rendered it unsuitable for the present purpose.

It is well known that the flow of a jet becomes turbulent only a short distance downstream from its exit. This seemed to offer an easily obtained turbulent flow field. The general aim was to investigate the traveling-shock-wave - turbulent-jet interaction. Various arrangements of different jets, mounted either outside or inside the shock tube, were tried. After some preliminary experiments, these efforts were abandoned in favor of the arrangement described.

Grids (or screens) are commonly used to produce isotropic turbulence fields in wind tunnels (refs. 8 and 9). By adapting this technique for use in the shock tube, controlled turbulent flows which were suitable for a detailed investigation could finally be produced.

When a traveling primary (incident) plane shock wave reaches the grid mounted in its path, it splits into reflected and transmitted shock waves. The drift mass flow associated with these waves becomes turbulent

after its passage through the grid. This turbulent contact surface and the associated wave pattern are consistently reproducible and thus can be systematically investigated if some suitable instrumentation is developed.

It was decided to use the hot-wire anemometer in conjunction with shadowgraphs.[1] At present, the experimental technique is capable of measuring the speeds of the incident shock wave as well as those of the transmitted and reflected shocks. From these three measurements one can calculate the pressure drop between regions 3 and 5 (figs. 1 and 2) for grids of various configurations and solidities and for different shock strengths (i.e., at different Reynolds and Mach numbers).

Other miscellaneous investigations, such as the shadowgraphic records of the emergence and growth of the transmitted and reflected shocks, the choking of grids, and the interaction of the turbulent contact surface with a reflected transmitted shock, are discussed. By the use of a hot-wire anemometer, the temperature and mass-flow characteristics of the flow fields associated with the transmitted shock wave and the turbulent contact surface are recorded and examined.

The author is indebted to Drs. Francis H. Clauser and Leslie S. G. Kovásznay for their encouragement and many helpful and stimulating discussions. Mr. Richard Swartley's help with the experimental work is appreciated.

This research was supported by the Office of Scientific Research of the Air Research and Development Command of the Department of the Air Force. The author wishes to express his sincere appreciation for this support.

The present report is essentially based on Part II of a dissertation (ref. 1) submitted by the author to the Faculty of Philosophy of the Johns Hopkins University in conformity with the requirements of the degree of Doctor of Philosophy. It has been made available to the National Advisory Committee for Aeronautics for publication because of its general interest. Part I of the dissertation has already been published by the NACA as Technical Note 3163 (ref. 2).

---

[1]The preliminary experimental observations of this work were presented by the author at an informal shock-tube meeting at Princeton University in January 1953. At the same meeting, Dr. I. I. Glass of the University of Toronto (Canada) showed a position-against-time schlieren of shock-screen interaction taken in a wave interaction tube. For subsequent developments of the shock-screen-interaction investigations by the research group at Toronto, see references 10 and 11.

SYMBOLS

A_{cr}	minimum critical cross section
A_o	total open area of grid
A_t	total area of grid
a	speed of sound (subscript indicates corresponding region of flow)
b	bar or wire width
b_{eff}	effective width between perforations in perforated plate or wire width in commercial screens
C_v	specific heat at constant volume
d	diameter of circular holes in grid
e	internal energy per unit mass of gas
k	pressure-drop coefficient
L_m	mesh length (see fig. 2)
M	Mach number
p	pressure
Re_3	Reynolds number based on B_{eff} as characteristic length
Δp	pressure drop, $p_3 - p_5$
S	strength of incident shock, p_2/p_1
S_R	strength of reflected shock, p_3/p_2
S_T	strength of transmitted shock, p_5/p_1
S_T'	strength of reflected transmitted shock, p_6/p_5
s	solidity ratio of a grid or screen
T	temperature

U speed of incident shock

U_R speed of reflected shock

U_T speed of transmitted shock

U' speed of totally reflected incident shock

U_T' speed of totally reflected transmitted shock wave when it advances against drift flow associated with transmitted shock front

$(U_T')_c$ speed of totally reflected transmitted shock wave when it advances against turbulent contact flow

u velocity of drift flow

γ ratio of specific heats

μ viscosity

ρ density

Subscripts:

1,2,3,4,5,6 regions of flow as shown in figures 1 and 2; for example, u_3, T_3, and so forth are parameters for region 3 which lies between upstream face of grid and reflected shock front

c contact flow

x distance downstream from grid

EXPERIMENTAL EQUIPMENT

The experimental equipment consisted of the following functional units:

(1) Shock tube

(2) Timing and triggering device

(3) Grids and their mounting

(4) Hot-wire equipment

(5) Arrangement for shadowgraphs

The equipment is the same as that described in references 1 and 2. Only a brief description will be given here.

Shock Tube

The shock tube consists of a steel box of uniform cross section (approximately 6 by 4 inches inside) which is divided into two chambers by a diaphragm across which a pressure differential can be sustained. The high-pressure side is called the compression chamber and the low-pressure side, the expansion chamber (fig. 3). The shock tube is laid with its 6-inch side horizontal, thus augmenting the effects of the disturbances in the density gradient because of the longer path of the beam of light through the disturbed region.

The total length of the shock tube is 29 feet. The grids are mounted between two glass sections about 16 feet downstream from the location of the diaphragm.

Timing and Triggering Device

The timing of shock speeds and synchronized triggering for shadowgraphs were achieved by the use of a hot-wire anemometer as a transducer. When the shock wave passed over the heated wire, its response to the sudden change in flow conditions resulted in the necessary electric pulse. The block diagram of the associated electric system is shown in figure 4. For details see reference 7.

Grids and Their Mounting

The following grids have been actually used:

(a) One-fourth-inch-thick perforated steel plate with sharp-edged holes of 0.25-inch diameter (reamed) and 25-percent solidity

(b) One-fourth-inch-thick perforated steel plate with sharp-edged holes of 0.512-inch diameter (reamed) and 25-percent solidity

These grids are shown in figure 5. They were mounted between two glass sections as shown in figures 6 and 7. This arrangement made it possible to record simultaneously the reflected shock wave upstream from the grid as well as the transmitted shock wave, turbulent contact surface, and any associated flow phenomena downstream from the grid.

The earlier arrangement did not include the second glass section and there was a bolt near the end of the glass section which shows up in some of the shadowgraphs reproduced (see fig. 8).

The grid was visible from outside through the glass windows (fig. 7). If the flying cellophane particles from the diaphragm got attached to the grid, thus blocking some orifices, they were blown off with a high-pressure jet of air. For open-end operation of the shock tube, this was rather easy. However, for closed-end operation of the shock tube and especially for high-strength incident shocks, it was quite frequently necessary to unbolt the end plate and blow out the cellophane particles from the shock tube and/or the grid.

Hot-Wire Equipment

The hot-wire equipment used in this investigation was designed by Dr. Leslie S. G. Kovásznay. It utilizes the constant-current arrangement for the operation of the hot-wire anemometer. The equipment consists of functional units such as control unit, calibration unit, and compensating amplifier assembled together. For detailed information see reference 12. The arrangement used to record oscillographically the response of the hot-wire to various flow regions is shown in figure 9.

Arrangement for Shadowgraphs

The point source of light for the shadowgraphs was provided by a sudden high-voltage discharge (about 6,000 volts) of six coaxially arranged condensers (total capacity of 0.12 microfarad) with a firing time of about 1 microsecond (ref. 13).

The synchronization of the firing of the spark with the arrival of the shock front at the desired location was achieved by setting a preestimated delay with the help of the preset delay generator which is actuated by the pulse from the triggering hot-wire (fig. 3).

Three different arrangements of the beam of light were tried:

(a) Divergent beam of light; that is, the source of light was used without any collimating lens (fig. 10).

(b) Parallel beam of light (collimated by Kodak f/4.5 lens with 12-inch focal length). The field of view was only about 2.6 inches in diameter (fig. 11).

(c) Parallel beam of light (collimated by a f/4.5 lens with 500-millimeter focal length). The field of view was approximately 4.4 inches in diameter (fig. 7). This arrangement made it possible to take shadowgraphic records covering the complete top-to-bottom section of the shock tube.

The optical arrangement used is indicated under every shadowgraph reproduced.

SCOPE OF INVESTIGATION

In the present investigation the following aspects of the problem were of main concern:

(a) The examination of the effects of the grids on the shock fronts and their subsequent behavior

(b) Determination of the pressure drop between locations "far" upstream and "far" downstream of the grid

(c) The interaction of the reflected transmitted shock front with the turbulent contact surface

(d) The use of the hot-wire anemometer for recording the characteristics of the various wave fronts and the associated flow fields on the downstream side of the grid

All these aspects are influenced by the grid geometry which can be varied by changing either the relative dimensions of the pattern elements or the pattern itself. The most common pattern used in a conventional wind tunnel is the square-mesh lattice formed by straight bars or wires evenly spaced in both directions. These two rectilinear sets of bars can be arranged in one or two planes. Commercial woven wires are also commonly used and they usually are intermediate between the single and the biplane types. Perforated plates are also frequently used (ref. 8).

In the shock-tube work the wire woven screens (ref. 10) and perforated plates are convenient to use. They can be easily mounted and can also be sealed for partial vacuum (fig. 6).

The solidity ratio s is the ratio of the total projected area of the solid parts of the grid exposed to the gas to the area of the grid boundary. When the grids are mounted perpendicular to the flow, the solidity ratio is

$$s = \frac{A_t - A_o}{A_t}$$

This essentially is the fractional degree to which the grid (or screen) obstructs the flow and is a measure of the relative scale of its pattern.

The pressure drop, that is, the energy change through the screen, is represented by the pressure-drop coefficient

$$k = \frac{\Delta p}{\frac{1}{2}\rho_3 u_3^2} = \frac{p_3 - p_5}{\frac{1}{2}\rho_3 u_3^2} \qquad (1)$$

where k is normally a function of Mach number, Reynolds number, solidity of the grid, and its pattern.

The Reynolds number is defined as

$$Re_3 = \frac{U_3 \rho_3 b_{eff}}{\mu_3} \tag{2}$$

where b_{eff} is the effective width between perforations in the case of a perforated plate or the wire width in the case of the commercial screens.

From figure 2, in the case of a square-lattice grid

$$\frac{\text{Open area}}{\text{Total area}} = \left(1 - \frac{b}{L_m}\right)^2 \tag{3}$$

In the case of the perforated plate

$$\frac{\text{Open area}}{\text{Total area}} = \frac{\pi \frac{d^2}{4}}{\sqrt{\frac{3}{2}} L_m^2} \tag{4}$$

Comparing relations (3) and (4)

$$b_{eff} = L_m - 0.952d \tag{5}$$

Where L_m is the mesh length (fig. 2).

ASSUMED WAVE MODEL AND ASSOCIATED FIELDS OF FLOW

After its collision with the grid, the incident shock wave gives rise to a transmitted shock wave (advancing downstream from the grid) and a reflected shock wave (advancing upstream from the grid). See figures 8(d) to 8(g). Very shortly after their disengagement from the grid, these shock fronts are distorted and are far from being plane and normal (fig. 12). The regions behind them are studded with crisscrossing shock

patterns which are caused by the diffraction of the primary shock over the solid parts of the grid. These diffraction shocklets, in turn, must have an associated complex system of rarefaction waves, which will naturally fan out as the flow progresses (figs. 8(e) and 8(g)).

The reflected shock wave moves upstream against the drift flow associated with the corresponding incident shock wave. However, the flow at the back of the reflected shock front moves downstream toward the grid. After its passage through the grid, this flow emerges as a system of multiple jets (figs. 8 and 12(f)). A short distance downstream these jets merge and subsequently their turbulent flow field covers the entire cross section of the tube.

When one considers that this is a transient phenomenon and highly unsteady near the grids, the complexity of any theoretical analysis of the problem is self-evident. However, the rapidity with which these fragmentary shock fronts (both transmitted and reflected) join and straighten up is surprising (see section "Structure of Transmitted and Reflected Shock Fronts") and their speeds thereafter seem to be quite constant.

To make the subsequent analysis of the experimental data possible, the wave model as reproduced in figure 1 is proposed. The various regions of the flow are numbered for later identification of the corresponding flow parameters.

This model rests on the following assumptions:

(1) The incident shock is plane, normal, and constant in strength.

(2) Beyond a short distance downstream from the grid, the transmitted shock is plane, normal, and constant in strength and has a uniform flow field behind it.

(3) The multiple jets issuing from the grid holes are fully contracted and essentially undiffused very close to the grid. In the very early course of their flow they mix, diffuse, and become turbulent. It is assumed that there is no pressure and particle velocity discontinuity between the turbulent contact region and the drift flow behind the transmitted shock wave.

(4) The transmitted shock when reflected, that is, the reflected transmitted shock, is also plane, normal, and constant in speed before it interacts with the turbulent contact surface.

(5) The reflected part of the incident shock is also plane and normal some very short distance upstream from the grid.

These assumptions imply that the effect of the secondary waves (diffraction shocklets and associated rarefactions) is ignored after the reflected and transmitted shocks are reasonably plane. These assumptions are obviously crude. Some observed deviations will be discussed later.

CONSIDERATION OF VARIOUS WAVE FRONTS AND ASSOCIATED FLOW FIELDS

The propagation of a constant-velocity shock wave in a homogeneous medium would appear as a steady process to an observer moving with the shock front. In this coordinate system and under the assumptions detailed in the preceding section, the gas motion associated with the traveling incident, reflected, and transmitted shock waves can be described by the conservation of mass, momentum, and energy equations of a plane, normal, and stationary shock front (ref. 14). The relations for the relevant flow parameters are summarized below.

Incident Shock Wave

In the case of the incident shock wave case the gas in front of the traveling shock front is at rest. Applying the standard known analysis of a stationary plane normal shock wave one gets

$$\frac{u_2}{a_1} = \frac{2}{\gamma + 1}\left(\frac{U}{a_1} - \frac{a_1}{U}\right) \tag{6}$$

and

$$\frac{u_2}{a_2} = \frac{2}{\gamma + 1}\left(\frac{a_2}{U - u_2} - \frac{U - u_2}{a_2}\right) \tag{7}$$

$$S = \frac{p_2}{p_1} = \frac{2\gamma}{\gamma + 1}\left(\frac{U}{a_1}\right)^2 - \frac{\gamma - 1}{\gamma + 1} \tag{8}$$

The corresponding Rankine-Hugoniot relation is

$$\frac{\rho_2}{\rho_1} = \frac{\frac{p_1}{p_2} + \frac{\gamma + 1}{\gamma - 1}}{\frac{\gamma + 1}{\gamma - 1}\frac{p_1}{p_2} + 1}$$

$$= \frac{1 + \frac{\gamma + 1}{\gamma - 1} S}{\frac{\gamma + 1}{\gamma - 1} + S}$$

$$= \frac{U}{U - u_2} \tag{9}$$

Also

$$\frac{a_2}{a_1} = \sqrt{\frac{T_2}{T_1}} = \sqrt{S\frac{\rho_1}{\rho_2}} \tag{10}$$

If the incident shock speed and the initial conditions in front of the shock are known, all of the gas parameters, such as u_2, M_2, ρ_2/ρ_1, p_2/p_1, and T_2/T_1, can be calculated (ref. 2).

Transmitted Shock Wave

The gas in front of the transmitted shock wave is also at rest. This shock front obeys relations similar to the incident shock. Therefore,

$$\frac{u_5}{a_1} = \frac{2}{\gamma + 1}\left(\frac{U_T}{a_1} - \frac{a_1}{U_T}\right) \tag{11}$$

$$\frac{u_5}{a_5} = \frac{2}{\gamma + 1}\left(\frac{a_5}{U_T - u_5} - \frac{U_T - u_5}{a_5}\right) \tag{12}$$

$$S_T = \frac{p_5}{p_1} = \frac{2\gamma}{\gamma + 1}\left(\frac{U_T}{a_1}\right)^2 - \frac{\gamma - 1}{\gamma + 1} \tag{13}$$

$$\frac{\rho_5}{\rho_1} = \frac{1 + \frac{\gamma + 1}{\gamma - 1} S_T}{S_T + \frac{\gamma + 1}{\gamma - 1}} = \frac{U_T}{U_T - u_5} \tag{14}$$

$$\frac{a_5}{a_1} = \sqrt{\frac{T_5}{T_1}} = \sqrt{S_T \frac{\rho_1}{\rho_5}} \tag{15}$$

If the speed of the transmitted shock wave and the initial conditions in front of it are known, all of the gas parameters, such as u_5, M_5, p_5/p_1, ρ_5/ρ_1, and T_5/T_1, can be calculated.

Reflected Shock Wave

The reflected shock front travels upstream against the drift flow generated by the incident traveling shock. However, behind this reflected shock wave the flow is directed toward the grid with an approach velocity u_3. The drift velocities u_2 and u_3 are directed opposite to the direction of advance of the reflected shock front (fig. 2). In the case of a totally reflected shock wave from a solid boundary (grid with solidity ratio $s = 1$) $u_3 = 0$.

Applying the considerations of a stationary plane normal shock wave to this reflected shock front, one gets

$$\frac{u_3}{a_2} = \frac{u_2}{a_2} - \frac{2}{\gamma + 1}\left(\frac{U_R + u_2}{a_2} - \frac{a_2}{U_R + u_2}\right) \tag{16}$$

$$S_R = \frac{p_3}{p_2} = \frac{2\gamma}{\gamma + 1}\left(\frac{U_R + u_2}{a_2}\right)^2 - \frac{\gamma - 1}{\gamma + 1} \tag{17}$$

$$\frac{\rho_3}{\rho_2} = \frac{1 + \frac{\gamma + 1}{\gamma - 1} S_R}{\frac{\gamma + 1}{\gamma - 1} + S_R} = \frac{U_R + u_2}{U_R + u_3} \tag{18}$$

$$\frac{a_3}{a_2} = \sqrt{\frac{T_3}{T_2}} = \sqrt{S_R \frac{\rho_2}{\rho_3}} \tag{19}$$

Since the Mach number of the flow approaching the grid is

$$M_3 = \frac{u_3}{a_3} = \frac{u_3}{a_2} \frac{a_2}{a_3} \tag{20}$$

by combining relations (16) to (20) one gets

$$M_3 = \left[\frac{u_2}{a_2} - \frac{2}{\gamma + 1} \left(\frac{U_R + u_2}{a_2} - \frac{a_2}{U_R + u_2} \right) \right] \sqrt{\frac{1 + \frac{\gamma + 1}{\gamma - 1} S_R}{S_R \left(\frac{\gamma + 1}{\gamma - 1} + S_R \right)}} \tag{21}$$

The transmitted shock wave is reflected from the closed far end of the shock tube. This reflected transmitted shock front travels upstream against the drift mass flow associated with the transmitted shock wave. With respect to the reflecting solid boundary (the closed end), its speed is given by

$$U_T' = a_1 \frac{2S_T + \frac{2}{\gamma - 1}}{\sqrt{\frac{2\gamma}{\gamma - 1} \left(\frac{\gamma + 1}{\gamma - 1} S_T + 1 \right)}} \tag{22}$$

If the experimental speed U_T of the transmitted shock wave is measured, then its strength S_T is known (relation (13)) and therefore the expected values of U_T' can be calculated. This also leads to the strength S_T' of the reflected transmitted shock.

Expression for Pressure-Drop Coefficient

From relation (18) one gets

$$\frac{p_3}{p_1} = \frac{p_2}{p_1} \frac{1 + \frac{\gamma + 1}{\gamma - 1} S_R}{\frac{\gamma + 1}{\gamma - 1} + S_R} \tag{23}$$

From relation (17) one gets

$$\frac{p_3}{p_1} = S\left[\frac{2\gamma}{\gamma + 1}\left(\frac{U_R + u_2}{a_2}\right)^2 - \frac{\gamma - 1}{\gamma + 1}\right] \tag{24}$$

From relations (16) and (23)

$$\frac{\rho_3 u_3^2}{\rho_1 a_1^2} = \left(\frac{a_2}{a_1}\right)^2\left[\frac{u_2}{a_2} - \frac{2}{\gamma + 1}\left(\frac{U_R + u_2}{a_2} - \frac{a_2}{U_R + u_2}\right)\right]^2 \frac{\rho_2}{\rho_1} \frac{1 + \frac{\gamma + 1}{\gamma - 1} S_R}{\frac{\gamma + 1}{\gamma - 1} + S_R} \tag{25}$$

From relations (13) and (24)

$$\frac{p_3 - p_5}{\rho_1 a_1^2} = \frac{p_1}{\rho_1 a_1^2}\left\{S\left[\frac{2\gamma}{\gamma + 1}\left(\frac{U_R + u_2}{a_2}\right)^2 - \frac{\gamma - 1}{\gamma + 1}\right] - \left[\frac{2\gamma}{\gamma + 1}\left(\frac{U_T}{a_1}\right)^2 - \frac{\gamma - 1}{\gamma + 1}\right]\right\} \tag{26}$$

From relations (25) and (26)

$$k = \frac{p_3 - p_5}{\frac{1}{2}\rho_3 u_3^2}$$

$$= 2\,\frac{\dfrac{p_1}{\rho_1 a_1^2}\left\{S\left[\dfrac{2\gamma}{\gamma+1}\left(\dfrac{U_R + u_2}{a_2}\right)^2 - \dfrac{\gamma-1}{\gamma+1}\right] - \left[\dfrac{2\gamma}{\gamma+1}\left(\dfrac{U_T}{a_1}\right)^2 - \dfrac{\gamma-1}{\gamma+1}\right]\right\}}{\left(\dfrac{a_2}{a_1}\right)^2\left[\dfrac{u_2}{a_2} - \dfrac{2}{\gamma+1}\left(\dfrac{U_R + u_2}{a_2} - \dfrac{a_2}{U_R + u_2}\right)\right]^2 \dfrac{\rho_2}{\rho_1}\,\dfrac{1 + \dfrac{\gamma+1}{\gamma-1}S_R}{\dfrac{\gamma+1}{\gamma-1} + S_R}} \qquad (27)$$

The theoretical values of U_R and U_T (and therefore k) will surely be some functions of the effective solidity ratio of the grid and the strength of the incident shock wave. Such an analysis is still lacking. From the measured incident shock speed U and the known initial operating conditions in the shock tube, the shock strength S and the flow parameters u_2 and a_2 are known. If one also knows the experimental values of U_R and U_T, the pressure-drop coefficient k can be calculated from relation (27) (see section entitled Determination of Pressure-Drop Coefficient" and fig. 13).

Determination of Reynolds Numbers

The operating Reynolds number has been defined as

$$Re_3 = \frac{\rho_3 u_3 b_{eff}}{\mu_3}$$

where b_{eff} is the characteristic length.

Depending upon the operating conditions in the expansion chamber and the incident shock strength, one can produce flows of different Reynolds number for the same grid. To find $\rho_3 u_3$ and μ_3 one makes use of the measured shock strengths of the incident and the reflected shock waves.

From relation (19) one gets

$$\frac{T_3}{T_1} = \frac{T_2}{T_1} S_R \rho_2/\rho_3$$

Knowing T_3, the corresponding μ_3 can be found from the tables in references 15 to 17. The calculated range of the values of the operating Reynolds numbers for the grid with holes of 0.25-inch diameter (fig. 5(a)) is given in figure 14. Note the marked effects the initial operating conditions of the shock tube have on the Reynolds number of the flow.

EXPERIMENTAL PROCEDURE

Essentially there are three different operations carried out:

(1) Measurement of the speeds of various shocks

(2) Shadowgraphic records

(3) Oscillographic records

The experimental arrangement was capable of handling all three operations simultaneously. However, for convenience of operation, only the speed of the incident shock wave (i.e., the time it took to traverse a known distance) and shadowgraph pictures taken after predetermined delay times were recorded simultaneously.

The hot-wire-response records were taken in conjunction with the speed measurement of the corresponding incident or transmitted shock wave.

For the evaluation of the various aspects of the shock-wave - grid interaction (e.g., the experimental determination of the pressure-drop coefficient k and the Mach number M_3 of the flow approaching the grid), one needs to know at least three different shock speeds:

(a) Speed of the incident shock wave

(b) Speed of the transmitted shock wave

(c) Speed of the reflected shock wave

Measurements of Speeds of Incident and Transmitted Shock Waves

The measurement of the incident and transmitted shock speeds can be conducted with the hot-wire anemometer used as a transducer for timing purposes (ref. 7 and fig. 4). For the arrangement of these transducers for incident-shock-speed measurement see reference 2.

In case of the transmitted-shock-speed measurement, most of the time the starting pulse was taken from a timing hot-wire mounted only 2 inches downstream from the location of the grid. The shadowgraphs taken close to the grid show that the transmitted shock was well formed by that station. The second timing hot-wire (for the stop pulse) was located about 30 inches farther downstream. For comparison, a few speed measurements were made with the first timing hot-wire located some 10 inches downstream from the grid. The author did not observe any definite difference in the speed of the transmitted shock.

Because there were only one chronograph and only one set of triggering units, speeds of the incident shock wave and the transmitted shock wave were measured separately. At one pressure setting the speed of the incident shock was recorded several times and the average taken. However, it may be pointed out that in consecutive measurements the scatter was negligible. The same procedure was followed for the transmitted shock.

If an additional set of triggering units (ref. 7) and one more chronograph had been available, then, of course, the simultaneous recording of the incident and transmitted shock speeds would not have presented any problem.

An alternative procedure was also possible. By mounting four hot-wires, two upstream and two downstream of the grid, and taking an oscillographic record of their differentiated output, the hot-wire technique can be extended to accommodate the simultaneous recording of the incident transmitted and reflected shock speeds.

Measurement of Speed of Reflected Shock

Since the hot-wire pickup device and the associated circuit as operated at present were not capable of measuring directly the time the reflected shock took to traverse the distance between two known stations, the following optical technique was resorted to.

The grid was mounted between two glass sections (each 12 inches long) at about 16 feet downstream from the diaphragm. The upstream

glass section had a graduated scale on which a pointer (ordinary sewing needle) was mounted such that it could be slid back and forth with its tip showing up in the shadowgraphs (fig. 15(a)).

Using incident shock waves of the same strength successfully for a number of times, the shadowgraphs of the corresponding reflected shock front were recorded at different locations (anywhere between 1 inch to 11 inches) upstream from the grid. This was easily achieved by adjusting the estimated delay time such that the reflected shock front should appear in the field of view of the collimated source of light and close to the prearranged position of the reference needle. Since the speeds of the different reflected shocks were not known, to start with, a trial and error method was followed. Later it was normally easy to estimate the required delay settings within a workable accuracy. The speeds of the reflected shock waves were calculated by measuring the distance apart of the two locations of the shock front for a known difference in time delay. When the difference of the two counts of the preset delay generator corresponding to two successive locations of the reflected shock front was taken, the effect of any inherent delay in the triggering system (ref. 7) was automatically canceled. When there were relatively strong incident shock waves, the reflected shock front exhibited curvature (fig. 15). The position of the shock front was always measured with reference to its central straight portion.

As each shadowgraph was taken, the time taken by the incident shock wave to traverse a known distance was simultaneously recorded. This served as a check on the strength of the successive incident shock waves. The reproducibility was excellent.

Since the transmitted shock is already calibrated against the incident shock, the speeds of all three main traveling shock fronts involved are known. Curves of shock velocities against incident shock strength are given in figure 16.

ANALYSIS OF DATA

Structure of Transmitted and Reflected Shock Fronts

When the incident shock reaches the grid, part of it is obstructed by the solid parts and part of it passes unobstructed through the holes in the grid. Just in front of the solid parts of the grid the reflected shocklets locally have higher pressures behind them than the transmitted parts which entered the holes. During equalization of this pressure difference, a systematic pattern of diffracted shock and rarefaction waves originates.

When the transmitted shock emerges from the grid, its front has essentially the same pattern as that of the grid. Because of the difference of pressure behind these emerging shocks and the dead-air region, there originates another diffraction shock and rarefaction pattern. The rarefaction waves very consistently follow the transmitted and reflected shock fronts and during the process of fanning out they seem to weaken the associated diffraction shocklets (fig. 8(g)) and to a certain extent they would weaken the main shock fronts also.[2]

The structure of the transmitted shock front can be examined by taking shadowgraphs such that the source of light is set at an angle to the traveling shock front (fig. 10). This can be done by using either a divergent beam of light or collimated light. If the principal axis of the divergent beam of light and the shock front are in line with each other, then the shock front itself does not reveal any structure (fig. 8(c)). This also is the case when the collimated beam of light is parallel to the shock front (figs. 8(e) and 8(g)). If the beam of light and the location of the shock are set at an angle to each other (fig. 10), then the shadowgraph reveals an interesting structure (figs. 8(a), 8(b), 8(d), and 8(f)).

The earlier arrangement had only one glass section and there was a bolt near the end (figs. 8(a), 8(b), and 8(c)) which obstructed the visibility. Later two glass sections (with grid between them) were used and the bolt near the end was eliminated. With this arrangement, it was possible to record simultaneously the reflected shock wave upstream from the grid as well as the transmitted shock wave and any allied flow phenomena downstream from the grid. Some very interesting shadowgraphs were taken (figs. 8(d) and 8(g)). The reproducibility of the flow and the wave pattern was extremely good.

The relevant data are listed under each shadowgraph reproduced here. The upstream face of the grid corresponds to zero delay time. This means that the time required by the incident shock to traverse the distance between the triggering station to the upstream face of the grid is calculated from its measured speed and discounted from the reading of the delay generator. Also, due allowance is made of the known inherent delay in the triggering system (ref. 7). The arrows in the shadowgraph indicate the direction of advance of the shock fronts.

The "Venetian blind" pattern in the shadowgraphs of the shock fronts (fig. 8) can be explained since each column of holes is represented by its corresponding projected shock front as a vertical line. The interval (displacement) between these lines is dependent on the geometry of the columns (cf. figs. 8(d) and 8(f)) and the inclination of the beam of light with respect to the shock front (cf. figs. 8(a) and 8(b)) and the

---

[2]Recently, perforated walls have been effectively used to alleviate the problem of shock-wave reflection in the working section of transonic tunnels (ref. 18).

location of the photographic film (fig. 10). The rows show up as cross-bands. There is a somewhat stronger pattern at the top and bottom. This was due to the asymmetric distribution of the solid parts at the top and bottom rows (figs. 8(a) to 8(c)). This was later somewhat improved by drilling additional holes in the upper and lower rows. However, the effect of the corners was not entirely eliminated (fig. 8(d)).

This "looking from behind" the shock front was frequently used to ascertain when a particular shock front became really plane. For instance, for the grid with larger holes (diameter of 0.512 inch), such shadowgraphs of the transmitted shock front did not reveal any waviness after about 7 inches downstream from the grid; that is,

$$\frac{x}{L_m} \approx 13$$

where x is the distance downstream from the grid and L_m is the mesh length (fig. 2). For a 1/4-inch-diameter-hole grid and the same shock strength, the shock front became plane at about 3 inches downstream (fig. 12(a)); that is,

$$\frac{x}{L_m} \approx 12$$

The grid with perforations of 1/4-inch diameter had 383 holes as against 95 for the one with perforations of 0.512-inch diameter. Therefore, in the case of the former grid, the wave pattern of the transmitted and the reflected shock fronts exhibits smaller displacement. Also, the diffraction shocklets in the wake of the shock fronts are comparatively more crowded. The structure of the wave fronts associated with the grid with larger diameter holes was thus more clearly discernible with the unaided eye and one could thus be comparatively more sure about the straightness of the shock front.

These observations were made with the expansion chamber operated at atmospheric pressure. If these experiments were carried on with the expansion chamber at reduced densities, then the optical resolution of the shadowgraphs is comparatively poor. By the same token the weaker shocks exhibit less marked distortion even near the grid (figs. 12(n) and 12(o)).

If a more precise determination of the position at which a particular shock front becomes "perfectly" plane is desired, it will be preferable to boost the optical sensitivity by the use of gases with higher refractive index than air (viz., Freon-12 and carbon tetrachloride (ref. 19)). This will also make it possible to examine, from shadowgraphs, the advance and mixing of the contact surface discontinuity

for periods longer than now possible with air-air operation of the shock tube having thick glass windows.

Determination of Pressure-Drop Coefficient

The pressure-drop coefficient was defined as

$$k = \frac{p_3 - p_5}{\frac{1}{2}\rho_3 u_3^2}$$

As detailed in the section "Experimental Procedure," the speeds of the incident, transmitted, and reflected shock fronts were measured, and, using the relations as discussed in the section "Consideration of Various Wave Fronts and Associated Flow Fields," the corresponding flow parameters ρ_3, u_3, p_3, and p_5 were calculated (figs. 17 to 19). The values of k corresponding to different shock strengths (i.e., different values of M_3 and Re_3) were determined and were plotted against M_3 (fig. 13). With increasing values of M_3, the pressure-drop coefficient k slowly decreases and when such incident shock strengths are reached that M_3 becomes constant (see the following section), k sharply increases. The same data were used for plotting $(p_3 - p_5)/\rho_3$ against u_3. This logarithmic plot could be closely approximated by a straight line and from its slope it was inferred that $(p_3 - p_5)/\rho_3$ varies approximately with the 1.5 power of the velocity u_3 (see ref. 20). After the grid exhibits choking (i.e., for $S \geqq 3.2$ and $u_3 = 676$ feet per second) the slope of the plot becomes sharply steeper. By using the data given in figures 17 to 19, one may also plot any other physically meaningful combination.

The present experimental setup did not lend itself for the determination of the pressure field just downstream of the grid. This pressure field is assumed eventually to attain equilibrium with the pressure field behind the transmitted shock. Therefore, k as defined here is not quite identical with the conventional pressure-drop coefficient across a grid (or screen).

An incident shock wave of a particular strength may be generated by several combinations of the initial pressures in the compression and expansion chambers provided the pressure ratio across the diaphragm is maintained the same. If the expansion chamber is operated at atmospheric pressure, then the Reynolds numbers Re_3 are considerably higher than the corresponding ones for the operation of the expansion chamber at

reduced pressures. Obviously, this wide variation in Re_3 is brought about by the difference in the density ρ_3 of the flow field in region 3. Corresponding to these different arrangements of operation of the shock tube, the Reynolds numbers Re_3 are plotted against incident shock strength S in figure 14.

No noticeable effects of expansion chamber pressure on the speeds of the incident, transmitted, and reflected shocks measured for the same pressure ratio across the diaphragm were observed.

This check on the effect of different operating Reynolds numbers but the same incident shock strength (i.e., same M_3) was possible only for $S \leq 2$. For higher incident shock strengths and open-end operation of the shock tube, excessive pressures in the compression chamber were needed. The compression chamber was capable of handling them, but the risk of cracking the glass plates in the working section stopped such an attempt. It may, however, be concluded that, within this limited range of S, if the grid is operated at the same Mach number M_3 but different Reynolds numbers Re_3, then there is no observable difference in pressure-drop coefficient k. Corresponding to weak incident shock waves (i.e., at very low Mach number M_3), the pressure drop $p_3 - p_5$ becomes so small a difference between two large quantities (fig. 18) that the experimental values of k are not reliable.

Observed Deviations from Assumed Wave Model

Auxiliary shock pattern and choking of grid.- As it is evident from relation (21), the Mach number of the flow approaching the grid (i.e., M_3) can be calculated if the state of the initial stationary medium in the shock tube and experimental values of U, the speed of the incident shock wave, and U_R, the speed of the reflected shock wave, are known. Such a procedure was systematically carried out for a considerable range of the incident shock strengths. It was found that for the grid used (fig. 5(a)) the Mach number M_3 assumes a fairly constant value; that is, $M_3 \approx 0.47$ (fig. 20) for incident shock strengths $S \geq 3.2$. For almost the same range of S values, an auxiliary shock front emerges out of the grid (fig. 21). It therefore follows that the grid is choked; that is, sonic speed is reached somewhere in the grid.

The structure of the emerging auxiliary shock pattern (fig. 21(a)) and its associated wave pattern (fig. 21(b)) follows the pattern of the grid itself. It is worth mentioning that the reflected shock front and this auxiliary shock front are similarly faced and that the transmitted shock is faced oppositely to them.

Successive shadowgraphs of the auxiliary shock front at increasing delay time settings were taken. They revealed that this auxiliary shock front is quite distorted and is being slowly washed downstream at gradually decreasing speeds. For instance, the auxiliary shock front corresponding to $S = 3.2$ moved downstream about 5/8 inch (distance between the downstream edge of the grid and the leading shocklet) in 1.3×10^{-3} second, that is, at an average speed of 40 feet per second (fig. 21(b)). In a subsequent shadowgraph (fig. 21(c)) the auxiliary shock front moved 1.5 inches in 4.33×10^{-3} second (i.e., an average speed of 29 feet per second). This also means that the auxiliary shock front took about 3.03×10^{-3} second to cover a distance 7/8 inch beyond its previous location and therefore had an average speed of 24 feet per second. It can therefore be inferred that the auxiliary shock front is gradually slowing down. However, in comparison with the corresponding particle velocity u_5 of 1,001 feet per second behind the transmitted shock (fig. 17), the speed of the auxiliary shock front is very small.

Behind the auxiliary shock front there also appears a diamond-shaped periodic wave structure. This demonstrates that the flow emerging out of the grid is supersonic. As measured from the original shadowgraphs recorded by the collimated source of light, the average horizontal and transverse diagonals of this repeating diamond pattern are 0.29 and 0.24 inch, respectively.

The observed choking of the grid is easily understood. The reflected shock builds up the pressure p_3 at the upstream face of the grid. The stronger the incident shock, the greater is the difference between p_3 and the pressure p_5 in region 5 behind the transmitted shock wave (fig. 18). Region 3 with its high pressure p_3 acts like a reservoir located upstream of the grid and the flow expands to lower pressure p_5. When the required critical pressure is reached, the grid chokes.

The grid holes (circular orifices) act like crude nozzles. At their exit the flow expands and develops an auxiliary shock front similar to a terminal shock in a supersonic wind tunnel. This auxiliary shock front is instrumental in boosting the pressure of the overexpanded flow out of the grid to the pressure in the region behind the transmitted shock wave.

The presence of a similar auxiliary shock is also observed behind a "Swiss cheese" grid projectile fired at supersonic speeds in a ballistic range (ref. 4).

The solidity ratio

$$s = \frac{A_t - A_o}{A_t}$$

is essentially the fractional degree to which the grid obstructs the flow in the shock tube. Imagine that the solid and the open parts of the grid are so arranged that, at the section in which the grid is mounted, they represent an idealized and symmetrical contraction and then enlargement of the cross-sectional area of the shock tube. The minimum cross section (say A_{cr}) thus created is equivalent to A_o, the total open area of the grid.

Further assume that one-dimensional isentropic flow conditions are still valid. These are obviously crude assumptions. However, the presence of an expansion through the grid makes the assumptions of isentropic flow a bit less unpalatable, especially prior to the advent of the choking phenomenon.

Under these assumptions one has at his disposal the standard area-ratio - Mach number relationship for an isentropic one-dimensional channel flow (ref. 21).

When the incident shock strength S (or M_3) reaches a certain critical value, the flow reaches Mach number 1 at the minimum cross section A_{cr} of the shock tube.

Therefore

$$\frac{A}{A_{cr}} = \frac{1}{M_3}\left(\frac{\frac{\gamma - 1}{2} M_3^2 + 1}{\frac{\gamma + 1}{2}}\right)^{\frac{\gamma + 1}{2(\gamma - 1)}} \tag{28}$$

If one experimentally measures U and U_R for some incident shock strength S for which the grid manifests choking, then the corresponding Mach number M_3 can be calculated from relation (21). Then by the use of relation (28) (and since $A_{cr} \equiv A_o$ and $A \equiv A_t$), the solidity ratio of the grid can be determined.

For the case in hand, the first indication of choking appeared at incident shock strength $S \approx 3.0$. The phenomenon was clearly established at $S = 3.2$ (fig. 21). The corresponding Mach number $M_3 \approx 0.47$ (fig. 20). The calculated solidity ratio $s = 0.29$. The grid used had a solidity ratio $s = 0.25$ (fig. 5). According to relation (28), the grid should have choked at $M_3 \approx 0.50$. Considering the bold assumptions involved, the agreement is surprisingly good. If one were to take into consideration the unavoidable boundary-layer effects in the orifices of the grid, the effective solidity of the grid would be bound to be somewhat larger than the one for which it is drilled.

This close agreement encourages one to presume that, for a grid of known solidity ratio, one should be able to predict, within a tolerable approximation, the value of the Mach number M_3 of the approaching flow at which the grid will get choked. However, a theoretical analysis leading to the prediction of the strength of the reflected and transmitted shock waves (as functions perhaps of the effective solidity ratio of the grid and the incident shock strength) would be very desirable.

Curving of reflected shock front.- One of the assumptions for the simplified analysis discussed in the section entitled "Consideration of Various Wave Fronts and Associated Flow Fields" was that the transmitted and the reflected shock fronts are plane and normal. It was experimentally demonstrated that within certain limits this assumption is quite realistic.

The shadowgraphs of the reflected shock recorded at "extended" distances (about 10 inches) upstream from the grid, however, reveal an appreciable curvature in the shock front. This is especially true of relatively higher incident shock strengths (figs. 15(d) and 15(e)).

The curvature originates near the walls where the "softening" of the shock front is quite evident (fig. 15(c)). Note that the curved part of the shock front leads the central straight part of the shock front. The farther upstream from the grid one records these shadowgraphs, the more pronounced are these effects.

Corresponding to stronger incident shock waves, it is observed that, even at relatively short distances upstream from the grid, the reflected shock front develops a λ type of bifurcation (see fig. 15(d)). Shadowgraphs of the same (strengthwise) shock front at later instances, that is, farther upstream, reveal that the λ bifurcation has progressed more toward the center and this λ configuration is undiscernibly "soft" in the region nearer the walls while the central part of the main shock front is appreciably curved (fig. 15(e)).

Obviously interaction of the shock wave and boundary layer is responsible for these distortions in the traveling reflected shock front. The drift mass flow $\rho_2 u_2$ associated with the traveling incident shock wave gives rise to boundary-layer flow near the walls (region 2, fig. 1). The thickness of this boundary layer at any particular location depends upon the total time the air particles, set in motion relative to the walls by the passage of the incident shock, have been in motion (ref. 22). The interval of time between the passage of the incident shock at some section upstream from the grid and the subsequent arrival of the reflected shock front at the same section is larger the farther upstream that section is located. Therefore it follows that the corresponding boundary-layer thickness will be comparatively greater at that section.

Also, the pressure behind the reflected shock front is appreciably higher than the one ahead of it. This adverse pressure gradient propagates through the boundary-layer regions (where the opposing particle velocity is slower) and is likely to increase the rate of thickening of the boundary layer ahead of the main reflected shock front. Therefore, farther upstream from the grid, the boundary-layer flow interacts with increasingly larger segments of the reflected shock front and eventually the observed curvature in the reflected shock front develops.

At higher shock strengths $S \geq 5$, especially at locations about 10 inches upstream from the grid, the reflected shock front becomes so distorted (fig. 15(e)) that the assumption of its being plane and normal (over the entire cross section) is no longer realistic. Perhaps a slight drop in the calculated M_3 corresponding to $S \approx 5.68$ is caused by such deviations. It could be that if incident shock waves of even higher strength were used this effect would increase.

Incidentally, all the shadowgraphs reproduced in figure 15 were recorded before the contact surface flow interacts with these traveling reflected shock fronts. Also, the influence of the diffracted shocklets originating because of some asymmetric distribution of the solid parts at the corners of the grid (fig. 8(d)) was considered of secondary importance and has been, therefore, overlooked in the above discussion.

Interaction of Reflected Transmitted Shock With Turbulent Contact Flow

The transmitted shock becomes quite plane and normal only a short distance downstream from the grid. It is reflected at the closed end of the shock tube. This reflected shock (referred to here as reflected transmitted shock) advances upstream against the drift flow ($\rho_5 u_5$) associated with the transmitted shock and eventually interacts with the turbulent contact flow.

Two arrangements were used to observe this interaction:

(a) The closed end of the shock tube was only about 1 foot (length of a single glass section) downstream from the grid.

(b) The grid was mounted such that the closed end of the shock tube was about 2 feet downstream from the grid. This was achieved by using two glass sections in series and mounting the grid between the first glass section and the steel section. Thin rubber gaskets were used to cushion glass-to-steel and glass-to-glass joints. This arrangement allowed a longer time of interaction between the reflected transmitted shock and the turbulent contact flow.

A sequence of shadowgraphs is reproduced to demonstrate the development of this interaction. The relevant data are listed under each shadowgraph.

The straightening up of the transmitted shock is demonstrated by its shadowgraph taken at only 3 inches downstream from the grid (fig. 12(a)). The planeness of this shock front, however, was checked by a corresponding shadowgraph recorded with an inclined beam of light (see section "Structure of Transmitted and Reflected Shock Fronts").

This transmitted shock front is reflected from the closed end of the shock tube located about 2 feet downstream from the grid. The reflected transmitted shock travels upstream against the drift flow (generated by the transmitted shock). Before it enters the turbulent contact region, the reflected transmitted shock front is quite plane, normal, and thin (fig. 12(b)). The wave pattern observed on both sides of this advancing shock front is the one originally linked with the transmitted shock wave.

The reflected transmitted shock front entered the contact flow at 11 inches downstream from the upstream face of the grid (fig. 12(c)). The corresponding delay reading (2,491 microseconds) for the reflected transmitted shock front was known. It was, therefore, possible to calculate the mean particle velocity $\left[(u_4)_c \approx 369 \text{ feet per second}\right]$ of the contact flow. Also, the corresponding drift velocity $(u_5 \approx 368$ feet per second) was calculated from the measured transmitted shock speed. The agreement was consistently good, thereby demonstrating the validity of the usual assumption $(u_4)_c = u_5$ across the contact flow.

Incidentally, part of the secondary wave pattern behind the shock front (fig. 12(c)) was associated earlier with the transmitted shock front. The cusp-shaped wave pattern originated because of some slight imperfection in the alinement at the joint between the two glass sections.

After the interaction of shock and turbulent contact flow has taken place for about 0.5 millisecond (distance advanced approximately 6 inches), the reflected transmitted shock front has moved to a location $4\frac{1}{4}$ inches downstream of the grid and its shadowgraph (collimated light beam normal to the glass windows) reveals considerable distortion and thickening (due to shadow effects) of the shock front.(fig. 12(d)). If the same (strengthwise) shock front is shadowgraphed from behind (collimated light beam at 4° inclinations to the shock front), then the internal distortions in the shock front are resolved (fig. 12(e)). The intense striations in this shadowgraph most likely manifest the local scale of random fluctuations in the flow. As measured from the original negative, the average length of the striations is roughly 1/4 inch. In a

similar shadowgraph of the reflected transmitted shock front taken farther downstream from the grid (similar to fig. 12(c) and not reproduced here) these striations were apparently less numerous and more diffused and their average length was roughly 0.5 inch.

As the reflected transmitted shock front advances toward the grid, it exhibits more regular distortions which conform to the general pattern of the grid (figs. 12(f) and 12(g)). This essentially is the region of unmixed jets issuing out of the array of the circular orifices in the grid. The regular "bulge" pattern in the shock segments facing the jets originated because of shock-jet interaction. The weak shocklets which appear slightly ahead of the main shock front most probably owe their existence to the shock - boundary-layer interaction. This inference is based on the observed fact that in the boundary-layer region (on all walls) the shock front pulls ahead of its central portion (fig. 15(c)).

Incidentally, the nature of the distortions of the reflected transmitted shock front seems to provide an interesting optical demonstration of mixing, spreading, and coalescing of these multiple adjacent jets. The presence of a regular pattern in the distorted shock front located at $1\frac{1}{4}$ inches (i.e., 5 mesh lengths) downstream from the grid establishes that the jets are yet not fully coalesced with each other (fig. 12(f)). However, if the shock front is located at about $4\frac{1}{4}$ inches (i.e., about 17 mesh lengths) downstream of the grid, the absence of any regular distortion pattern indicates that the jets are completely mixed and that turbulent contact flow fills the entire cross section of the shock tube. It may be added that the shadowgraph of the shock front taken at 2 inches (i.e., 8 mesh lengths) downstream of the grid also did not exhibit any well-defined distortion pattern. One could, therefore, reasonably infer that in the present case the multiple jets coalesce after an equivalent distance of approximately 6 mesh lengths.

From the set of shadowgraphs of the same (strengthwise) transmitted shock wave, some typical shadowgraphs of the reflected transmitted shock traveling against the turbulent contact flow were selected in pairs. From the difference between the known location of the shock front (i.e., distance traveled by the shock) and the corresponding difference between the preset delay readings (i.e., the corresponding time interval) the average experimental speed of the reflected transmitted shock $\left(U_T'\right)_c$ can be calculated. For instance, the shock fronts in shadowgraphs 12(c) and 12(g) were located 10 inches apart and the difference between their

corresponding delay times was 809 microseconds, thus giving an average $\left(U_T'\right)_c$ of 1,032 feet per second.

The same procedure was extended to calculate U_T', the speed of the reflected transmitted shock front traveling against the drift velocity u_5. From the combination of the shadowgraphic data in figs 12(a) and 12(b), the speed of the reflected transmitted shock front was calculated (U_T' = 1,086 feet per second). Since the experimental speed of the transmitted shock in figure 12(a) was known, the time of its arrival at the closed end was calculated and subtracted from the corresponding total delay reading of 2,320 microseconds for the reflected transmitted shock front in figure 12(b). The remainder (842 microseconds) was the time the reflected transmitted shock front took to travel from the closed end to its location, that is, a distance of $10\frac{31}{32}$ inches, including the thickness of the rubber gasket between the end plate and the glass section. The speed U_T' of the reflected transmitted shock front was also calculated from the successive shadowgraphs of the reflected transmitted shock alone. The scatter in the observed speeds of the reflected transmitted shock front was insignificant. The expected U_T' was determined from the experimental speed U_T of the transmitted shock (see relations (13) and (22)).

The comparison between U_T' and $\left(U_T'\right)_c$ is tabulated below. The calculations are based on the data collected by using the grid with diameter of holes equal to 0.25 inch and solidity ratio s = 0.25 for a single incident shock strength.

S	S_T	Shadowgraphs used	Observed U_T', ft/sec	Expected U_T', ft/sec	Observed $\left(U_T'\right)_c$, ft/sec
1.58	1.55	12(a), 12(b)	1,086 ± 5	1,089 ± 2	----------
1.58	1.55	12(c), 12(d)	1,086 ± 5	1,089 ± 2	1,041 ± 20
1.58	1.55	12(c), 12(f)	1,086 ± 5	1,089 ± 2	1,055 ± 20
1.58	1.55	12(c), 12(g)	1,086 ± 5	1,089 ± 2	1,032 ± 20

It may be worthwhile to point out that while shadowgraphing the step-by-step advance of the reflected transmitted shock front in the contact flow it was observed that in two successive shadowgraphs of the same reflected transmitted shock front, recorded by keeping the delay and the incident shock strength the same, the shock front would appear at slightly different locations. This random scatter was more apparent the farther upstream and the nearer to the grid the shock front was shadowgraphed. For the incident shock strength $S = 1.58$, the maximum scatter observed was $\pm 1/8$ inch (i.e., equivalent to ± 10 microseconds). The observed scatter in the recorded time interval for the incident and transmitted shock speed was seldom more than ± 1 microsecond in a time interval of over a millisecond. (The incident shock ($S = 1.58$) took, on the average, 1,182 microseconds to cover a distance of 19.7 inches between two timing hot-wires.) Any variations in the incident shock strength, however slight, have been taken into account and the data (such as delay time) refer to a single incident shock strength $S = 1.58$. Also, the reproducibility (locationwise) of the reflected transmitted shock before it enters the contact flow was very consistent. Therefore, the observed randomness in the location of the reflected transmitted shock could not be attributed to some erratic behavior of the electric system. It may, therefore, be conjectured that the state of the turbulent contact flow is instrumental in introducing the observed scatter in the speed of the reflected transmitted shock front. Even if this scatter is taken into account, it will at most change the observed speeds of the reflected transmitted shock front by ± 2 percent. The average observed reduction in the reflected transmitted shock speed U_T' due to its passage through the turbulent contact flow is about 5 percent. Therefore, one can infer that shock-wave and turbulent-flow interaction results in some dissipation of the shock strength. Since the complete data for such calculations were available for only one incident shock strength (i.e., $S = 1.58$), the above conclusion should be considered tentative.

(The importance of the shock-turbulence interaction (especially for its contribution toward aerodynamic noise generation) has been brought sharply into focus by recent publications of Lighthill, Ribner, and Kovásznay (refs. 23 to 25) and others. Applying Lighthill's analysis of the weak shock-turbulence interaction to the present case where $S_T' = p_6/p_5 = 1.51$, the total energy scattered by shock-turbulence interaction is approximately $8(S_T' - 1)/3\gamma(\gamma + 1)$ times the kinetic energy of turbulence traversed by the shock. The scattered energy will normally be expected to manifest itself as sound energy. Since the local speed of sound a_6 is greater than the speed $(U_T')_c$ of the shock front, most of the scattered energy will catch up with the shock front and be absorbed by it.)

(The freely scattered energy is given as a fraction of the kinetic energy of turbulence traversed by the shock wave:

$$0.7\left(S_T' - 1\right)^{3/2} - 1.0\left(S_T' - 1\right)^2 + 0.7\left(S_T' - 1\right)^{5/2}$$

For $S_T' \approx 1.51$, approximately 10 percent of the energy of turbulence traversed by the shock front should, therefore, be freely scattered. However, in spite of the intense mass fluctuations in the contact-flow region (roughly 15 percent of the steady mass flow $\rho_4 u_4$ (see refs. 2 and 3 and fig. 23(a)), the shadowgraphs of the shock-turbulence interaction did not exhibit any distinct sound scattering in the region behind the shock front (figs. 12(d) and 12(j)).)

It is regretted that only one glass section was effectively utilized for observing the interaction of turbulent contact flow and shock. It would have been worthwhile so to arrange the closed end of the shock tube that the reflected transmitted shock wave was made to enter the contact flow farther downstream from the grid. Thus the interaction could have been extended over longer periods covering the total span (24 inches) of both glass sections.

There is one aspect of the problem which still remains to be pointed out. From experimental observations (see section entitled "Oscillographic Records") it has been established that the contact front represents a temperature (and therefore density) discontinuity such that $\frac{\left(T_4\right)_c}{T_5} > 1$ where $\left(T_4\right)_c$ is the mean temperature of the contact flow and T_5 is the mean temperature of the drift flow behind the transmitted shock wave. Since the gas on both sides of the contact front is air and the operating shock strengths are moderate, it is reasonable to assume that γ and C_v, the specific heat at constant volume, are constant. It means that the ratio of the internal energies per unit mass of the gases across the contact front is equivalent to the corresponding temperature ratio. Therefore $\frac{\left(e_4\right)_c}{e_5} > 1$ where e stands for the internal energy per unit mass of the gas.

When the reflected transmitted shock front collides with this type of energy discontinuity across the contact front, the so-called absorption of the incident shock takes place; that is, a rarefaction wave and a new contact surface originate (not shown in fig. 1) and the transmitted part of the reflected transmitted shock front is weaker (i.e., slower in speed) than its precollision strength (see refs. 6 and 26 for details).

Such a rarefaction wave was not observed. (See, however, legend of fig. 12(c).) It is true that the shadowgraphic technique is not best suited for such an observation. However, some similar investigations of the interaction of the reflected shock and the usual contact front (the gas originally in the compression chamber) normally encountered in air-air operations of a shock tube are described in reference 6. Since there is a sharp downward temperature jump across the contact front (for the experimental demonstration of this fact see fig. 15 in ref. 2 and fig. 5 in ref. 7), the ratio of the internal energies per unit mass of the gases across the contact front is less than 1. This favors amplification of the incident shock and the origin of a reflected shock and a new contact surface. In spite of the fact that this interaction was observed when the downward temperature jump across the contact front was as high as 500° C, it is reported that no reflected shock was noticed (ref. 6).

It would not, therefore, be surprising if the expected rarefaction does not manifest itself in the present case where an upward temperature jump of only a few degrees (about 5° C corresponding to $S = 1.58$ and $T_5 \approx 41^\circ$ C) occurs. It is further believed that this temperature discontinuity across the contact front in the shock-grid interaction experiments, though sizable in comparison with values of T_5 for weak incident shock waves, will always stay comparatively small in absolute magnitude. As the incident shock strength S is increased, both the transmitted and reflected shock front gain in strength. Therefore, while $\Delta p = p_3 - p_5$ increases, the corresponding temperature T_3 (equivalent to the usual reservoir temperature in the operation of a wind tunnel or temperature of compression chamber in the normal operation of a shock tube) also progressively increases. This will tend to keep the temperature discontinuity $\Delta T = (T_4)_c - T_5$ across the contact front comparatively small. It, therefore, does not seem like a drastic simplification if the observed weakening of the reflected transmitted shock front is attributed primarily to the turbulent flow and shock interacting and the contribution of the temperature rise across the contact is considered secondary. One should, however, be cautious about extending this simplification to observations made in the expansion region in the very neighborhood of the grid.

For the grid with holes of diameter of 0.512 inch and solidity ratio s of 0.25, a similar sequence of shadowgraphs is reproduced (figs. 12(h) to 12(o)). The incident shock strength is $S = 1.387$. Only one glass section (12 inches long) was then available. Therefore, the reflected shock front entered the turbulent contact flow at about 5 inches downstream from the grid. The interaction time was obviously shorter than that for the arrangement discussed above. This is one of the reasons why the second glass section was built. Since the experimental speed

of the transmitted shock was not recorded, the comparison between $(U_T')_c$ calculated from the shadowgraph data reproduced here and the "expected" U_T' was not possible.

If the reflected transmitted shock front is followed until it collides with the grid, it splits into its transmitted and reflected parts. The reflected part looks very weak and disconnected near the grid (fig. 12(l)) but later on forms into a wave front (fig. 12(m)) which moves downstream with an average speed of about 808 feet per second.

The shadowgraphs of the reflected transmitted shock of different strengths near the same grid (figs. 12(k) and 12(o)) demonstrate that the distortions are more pronounced in the case of the stronger shock front. The reflected transmitted shock front corresponding to $S = 1.387$ (fig. 12(k)) exhibits a strongly "shredded" shock front, while the reflected transmitted shock front corresponding to $S = 1.09$ has developed only a gentle sinusoidal shape (fig. 12(o)). It may, however, be added that, corresponding to the weaker shock, the optical sensitivity is considerably reduced. In some shadowgraphs the apparent fluctuation level at the back of the shock front seems to be somewhat enhanced (figs. 12(f) and 12(j)). Considering the higher density level behind the shock, this, too, may be an optical effect.

OSCILLOGRAPHIC RECORDS

The hot-wire anemometer has been used to investigate the flow behavior behind the grids. The passage of a transmitted shock wave over the hot-wire is demonstrated in figure 22. Two typical oscillograms of the hot-wire response to the traveling transmitted shock front and the subsequent flow field are reproduced (fig. 23).

Depending upon its operating conditions, the hot-wire anemometer is sensitive to temperature and/or mass-flow fluctuations. For one of the oscillograms (fig. 23(a)), the hot-wire is operated at considerable initial temperature (i.e., large current through the wire; for relevant data see fig. 23) and is therefore predominantly sensitive to mass-flow fluctuations. For the other oscillogram (fig. 23(b)), the hot-wire is only slightly heated (i.e., small current through the wire) and it is therefore sensitive mainly to temperature fluctuation in the flow. The hot-wire is oriented perpendicular to the mean-flow direction and is located $1\frac{9}{16}$ inches downstream of the grid at the center of the shock-tube cross section.

The response of a hot-wire represents the time history of the flow at the location of the wire. It is evident from these oscillograms that, when the transmitted shock reaches the hot-wire, there is a sudden jump (segment A in fig. 23) which is followed by the hot-wire

response to the drift flow in region 5, which is bounded by the transmitted shock wave and the contact flow front.

This drift flow in region 5 is composed of the mass of air initially at rest downstream of the grid. Knowing the experimental speed of the transmitted shock, the particle velocity u_5 can be calculated from relation (11) (fig. 17). Therefore, if the location of the hot-wire downstream from the grid is known, the expected time interval Δt between the passage of the shock front and the subsequent arrival of the contact front at the hot-wire can be calculated. For the case in hand $u_5 = 368$ feet per second (fig. 17), and the distance between the downstream face of the grid and hot-wire is $1\frac{9}{16}$ inch; therefore the expected $\Delta t = 354$ microseconds. The corresponding Δt, as measured from the oscillograms (fig. 23), is approximately 350 microseconds. This close agreement means that even very close to the grid the drift velocity generated by the passage of the transmitted shock is almost equal to that generated by it farther downstream. This observation, therefore, supports the assumption made in the section entitled "Assumed Wave Model and Associated Fields of Flow" that the transmitted shock front attains constant velocity (or strength) only a short distance downstream from the grid.

Corresponding to the contact flow (segment B in fig. 23), the hot-wire response exhibits fluctuations. Beside the distinct and appreciable jump concurrent with the arrival of the turbulent contact front at the hot-wire, there also appear a number of small subsequent secondary jumps due to fluctuations in the level of the mean temperature and mass flow. These jumps are correlated (timewise) between the temperature and mass-flow oscillograms and the smaller ones are probably caused by multiple diffraction wavelets from both sides of the grid. The base trace in these oscillograms (i.e., D in fig. 23) indicates the noise level of the equipment at the operating conditions before the shock is generated and the sinusoidal wave C serves as the calibration signal for both amplitude and time.

The temperature oscillogram (fig. 23(b), segment B) reveals that the mean temperature $(T_4)_c$ in the turbulent contact flow is somewhat higher than the corresponding mean temperature T_5 of the flow behind the transmitted shock and that $(T_4)_c$ drifts upwards with the increasing time.

From the corresponding mass-flow oscillogram (fig. 23(a), segment B) it is observed that, concurrent with the arrival of the contact front at the hot-wire, there is a stepdown jump in the level of the signal. This sudden reduction in the negative signal level is perhaps due to the effect of the reduced mass flow and/or increased mean temperature in the contact flow. Both these effects will influence the mass-flow jump in the same direction. The turbulent contact flow (fig. 8) is composed of

the air upstream from the grid in region 3. This mass of air is twice "shocked" (by the incident and the reflected shocks) before it flows through the grid and thrice "shocked" after the choking state is reached. Therefore, its starting temperature, density, and pressure are higher and its particle velocity is lower than the corresponding flow parameters of region 5 (figs. 17, 18, and 19). Since at the interface the conditions $(p_4)_c \longrightarrow p_5$ and $(u_4)_c \longrightarrow u_5$ have to be satisfied, an expansion through the grid is inevitable. However, in spite of this expansion, $(T_4)_c$ is still greater than T_5 by about 5° C. It therefore follows that $(\rho_4)_c < \rho_5$ (see ref. 10). Incidentally, this demonstrates that the nature of this contact flow is opposite to the usual contact flow encountered in a shock tube (see section entitled "Interaction of Reflected Transmitted Shock With Turbulent Contact Flow").

By operating the same hot-wire at two different initial temperatures for the same shock strength (fig. 23), the temperatures of the flow behind the transmitted shock waves were calculated for shock strengths $S \leq 1.6$ (for details of procedure, see ref. 2). These temperatures were also calculated from relation (15) by using the experimental speeds of the transmitted shocks. The agreement was quite satisfactory.

By operating the same hot-wire at three different initial operating temperatures for the same shock strength, it is feasible to separate the mean-mass-flow and temperature jumps and also the level of the temperature and mass-flow fluctuations and their correlations (refs. 2 and 27).

The hot-wire is operated here in a constant-heating-current arrangement. If the initial operating temperature of the hot-wire is substantially higher than the expected temperature of the flow associated with the transmitted shock, then, after the passage of the shock front, the hot-wire temperature falls. This reduces its sensitivity to any subsequent mass-flow fluctuations. It is believed that, if this were not so, the observed stepdown jump corresponding to the arrival of the contact flow would have been more substantial (see fig. 23(a), segment B).

The constant-temperature operation of the hot-wire is a comparatively better technique when a flow with such large fluctuations is under investigation. Since only constant-current hot-wire equipment was available, an attempt was made to combine the functions of the constant-current and constant-temperature operation of a hot-wire. The heating current, in the hot-wire equipment used, was controlled by power tubes with a multiple bridge as the cathode load. It was possible, therefore, to superimpose a suitable voltage pulse to the control grid of the power tube and increase the current through the hot-wire, thus increasing its temperature and effective sensitivity.

To achieve this, a univibrator was used as the source of a rectangular voltage pulse which was coupled to the control grid of the

power tube. The triggering of the univibrator should be so synchronized that, just after the passage of the transmitted shock over the hot-wire, the additional current passes through the hot-wire. The duration of this quasi-stable state (i.e., delay time) should be such that the additional current is cut off before the flow slows down; otherwise, the wire will be burned. Preliminary trial of this arrangement was encouraging, but no experimental data were collected.

The head-on hitting of the hot-wire by the flying cellophane pieces of the diaphragm used to be a major cause of hot-wire failures. The presence of the grid in the path of these flying pieces eliminated this difficulty and it was therefore possible to use the same hot-wire over an extended period.

CONCLUDING REMARKS

For investigating the various aspects of the interaction of traveling shock waves with grids mounted in their path in a shock tube, the combined use of the shadowgraphic and hot-wire techniques has proved quite fruitful and reliable. The investigation of the nature of the turbulent contact flow and its effect on the velocity of the reflected transmitted shock front could be extended without any significant alteration in the present experimental arrangement.

However, by incorporating some of the suggested improvements in the timing and triggering equipment and by substituting a constant-temperature hot-wire set with a high frequency range, the scope of this investigation could be considerably enlarged.

When very weak incident shock waves were used and/or when the shock tube was operated at low densities, the sensitivity of the optical system to any flow fluctuations was considerably reduced. Even for this low-density operation a hot-wire anemometer will still respond to any transient fluctuations in the flow field - a decided advantage over the optical arrangements.

The Johns Hopkins University,
Baltimore, Md., May 9, 1955.

REFERENCES

1. Dosanjh, Darshan S.: I - Use of a Hot-Wire Anemometer in Shock Tube Investigations. II - The Interaction of Traveling Shock Waves With Grids. Ph.D. dissertation, The Johns Hopkins Univ., 1953.

2. Dosanjh, Darshan Singh: Use of a Hot-Wire Anemometer in Shock Tube Investigations. NACA TN 3163, 1954.

3. Kovásznay, Leslie S. G., and Clarken, Patricia C.: Experimental Investigations of Optical Methods for Measuring Turbulence. Dept. of Aero., The Johns Hopkins Univ.

4. Uberoi, Mahinder S., and Kovásznay, Leslie S. G.: Analysis of Turbulent Density Fluctuations by the Shadow Method. Jour. Appl. Phys., vol. 26, no. 1, Jan. 1955, pp.

5. Lobb, R. K.: A Study of Supersonic Flows in a Shock Tube. Rep. No. 8, Inst. Aerophys., Univ. of Toronto, May 1950.

6. McKee, R. M.: An Experimental Study of the Interaction of a Plane Shock Wave With a Contact Region. Tech. Note 1, Inst. Aerophys., Univ. of Toronto, Sept. 1954.

7. Dosanjh, Darshan S.: Use of a Hot-Wire for Transient Flow Phenomena. Rev. Sci. Instr., vol. 26, no. 1, Jan. 1955, pp. 65-70.

8. Baines, W. D., and Peterson, E. G.: An Investigation of the Flow Through Screens. Trans. A.S.M.E., vol. 73, no. 5, July 1951, pp. 467-480.

9. Eckert, B., and Pflüger, T.: The Resistance Coefficient of Commercial Round Wire Grids. NACA TM 1003, 1942.

10. Glass, I. I., and Patterson, G. N.: A Theoretical and Experimental Study of Shock-Tube Flows. Jour. Aero. Sci., vol. 22, no. 2, Feb. 1955, pp. 73-100.

11. Dosanjh, Darshan S.: Some Comments on a Theoretical and Experimental Study of Shock Tube Flows. Reader's Forum, Jour. Aero. Sci., vol. 22, no. 11, Nov. 1955, pp. 797-799.

12. Kovásznay, Leslie S. G.: Development of Turbulence-Measuring Equipment. NACA Rep. 1209, 1954. (Supersedes NACA TN 2839.)

13. Kovásznay, Leslie S. G.: High Power Short Duration Spark Discharge. Rev. Sci. Instr., vol. 20, no. 9, Sept. 1949, pp. 696-697.

14. Lukasiewicz, J.: Shock Tube Theory and Applications. Rep. No. MT-10, Nat. Res. Council (Canada), Jan. 18, 1950.

15. Morey, F. C.: Dry Air - Coefficients of Viscosity η/η_0, ν/ν_0. NBS-NACA Tables of Thermal Properties of Gases, Table 2.39, Dec. 1950.

16. Nuttall, R. L.: Dry Air - Thermal Conductivity k/k_0. NBS-NACA Tables of Thermal Properties of Gases, Table 2.42, Dec. 1950.

17. Hilsenrath, Joseph: Dry Air - Prandtl Number c_p/k. NBS-NACA Tables of Thermal Properties of Gases, Table 2.44, July 1950.

18. Allen, H. Julian: Transonic Wind Tunnel Development of the National Advisory Committee for Aeronautics. Paper presented at sixth meeting of Wind Tunnel and Model Testing Panel (Paris, Nov. 2-6, 1954), AGARD Memo. AG17/P7, Nov. 1954, pp. 198-217.

19. Duff, R. E.: The Use of Real Gases in the Shock Tube. Rep. 51-3, Eng. Res. Inst., Univ. of Mich., Mar. 1951.

20. Stokes, George M., Davis, Don, Jr., and Sellers, Thomas B.: An Experimental Study of Porosity Characteristics of Perforated Materials in Normal and Parallel Flow. NACA TN 3085, 1954.

21. Ferri, Antonio: Elements of Aerodynamics of Supersonic Flows. The Macmillan Co., 1949, Ch. I.

22. Donaldson, Coleman duP., and Sullivan, Roger D.: The Effect of Wall Friction on the Strength of Shock Waves in Tubes and Hydraulic Jumps in Channels. NACA TN 1942, 1949.

23. Lighthill, M. J.: On the Energy Scattered From the Interaction of Turbulence With Sound or Shock Waves. Proc. Cambridge Phil. Soc., vol. 49, pt. 3, July 1953, pp. 531-549.

24. Ribner, H. S.: Shock-Turbulence Interaction and the Generation of Noise. NACA TN 3255, 1954.

25. Kovásznay, Leslie S. G.: Interaction of a Shock Wave and Turbulence. Paper presented at 1955 Heat Transfer and Fluid Mech. Inst. (Univ. of Calif., Los Angeles, June 1955), 1955.

26. Ford, C. A., and Glass, I. I.: An Experimental Study of One-Dimensional Shock-Wave Refraction. Readers' Forum, Jour. Aero. Sci., vol. 23, no. 2, Feb. 1956, pp. 189-191.

27. Corrsin, Stanley: Extended Applications of the Hot-Wire Anemometer. NACA TN 1864, 1949.

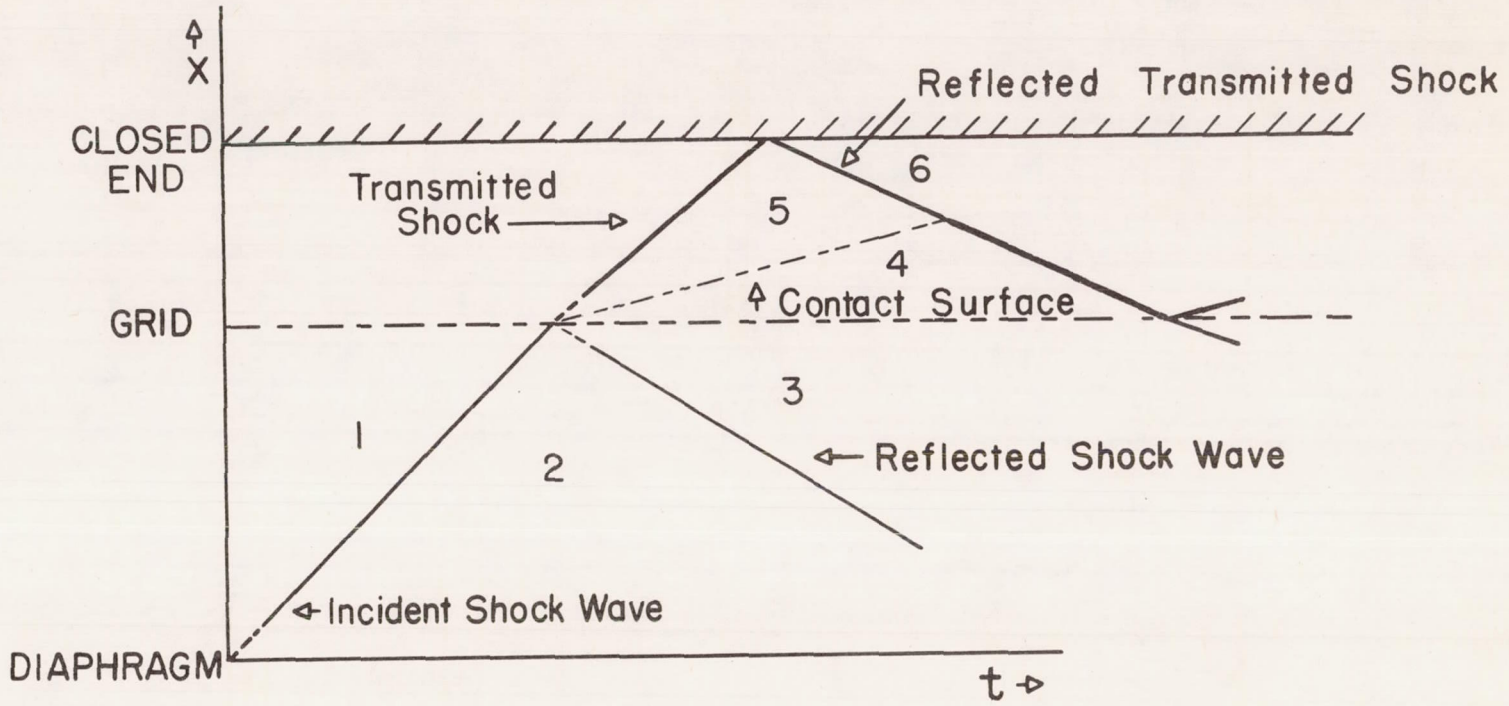

Figure 1.- Assumed wave model for interaction of shock wave and grid. x, distance downstream from diaphragm located at $x = 0$; t, time after diaphragm is ruptured at $t = 0$.

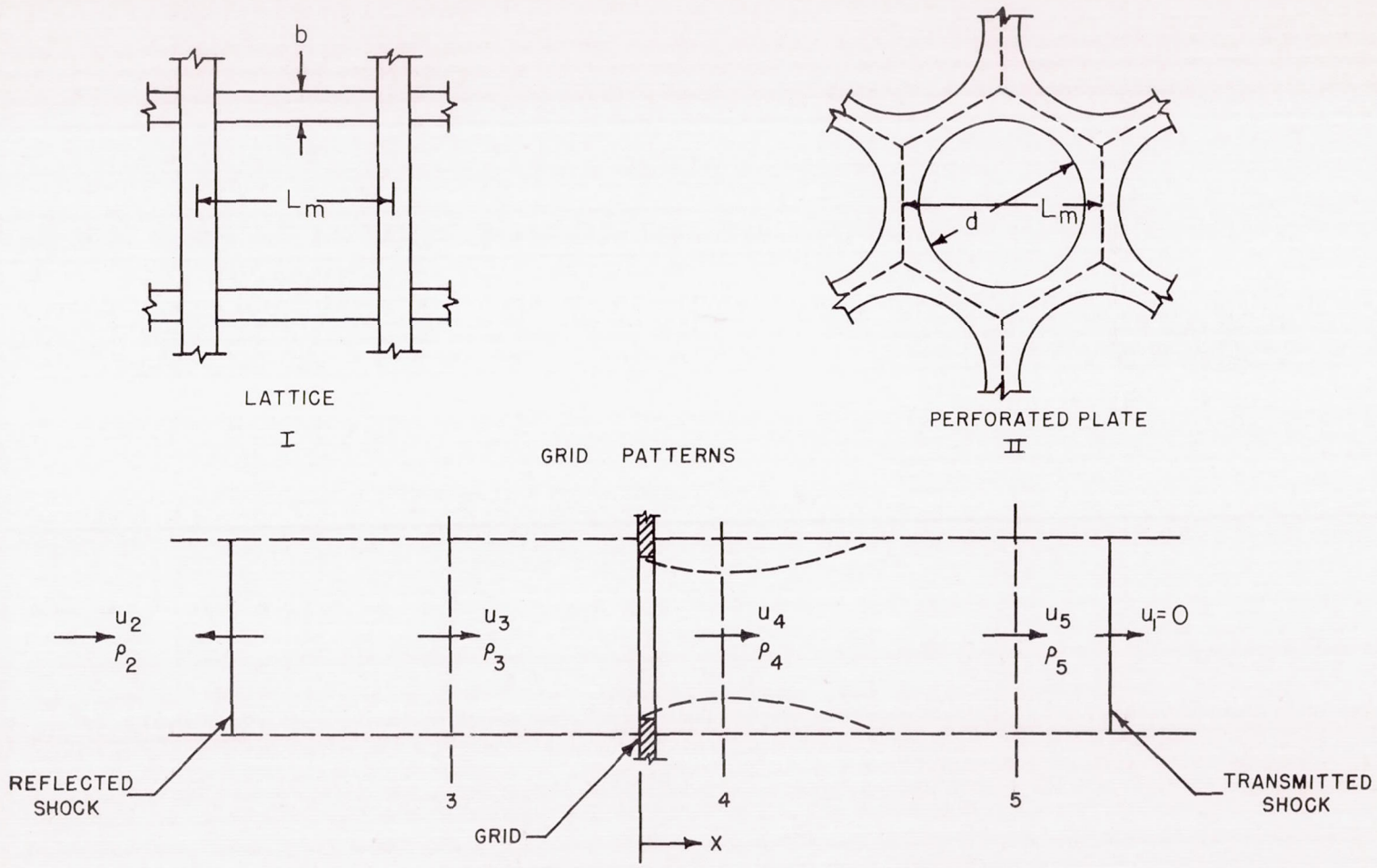

Figure 2.- Sketch showing various flow regions.

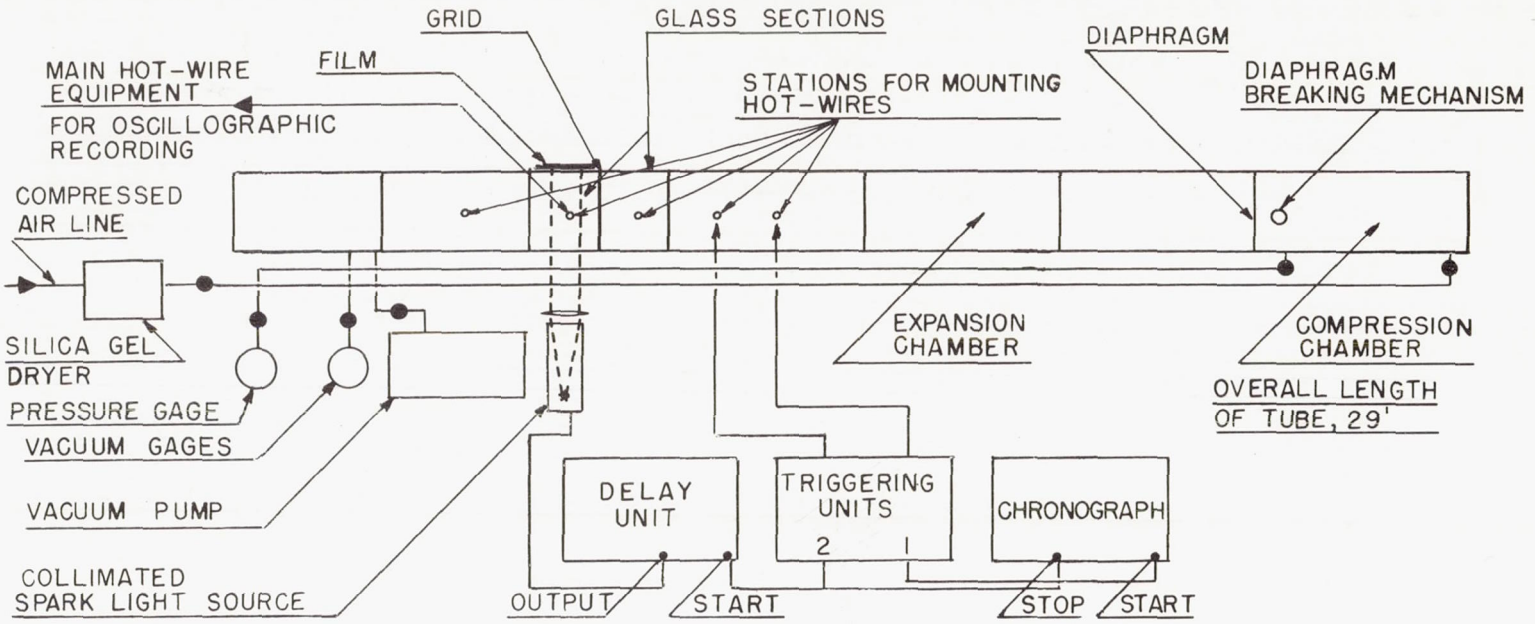

Figure 3.- Shock tube.

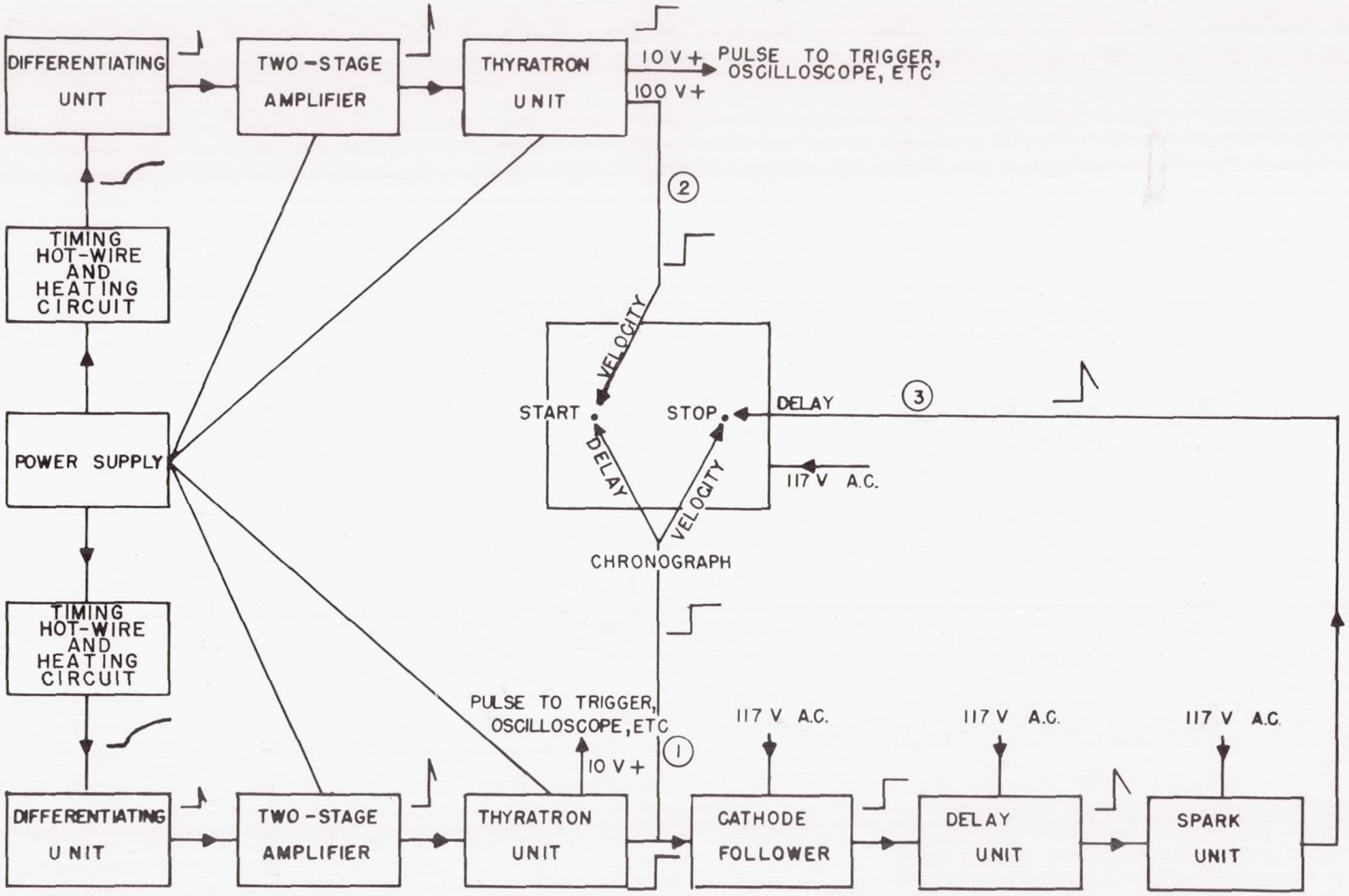

Figure 4.- Arrangement for measuring shock speeds or setting and recording time delay for shadowgraphs.

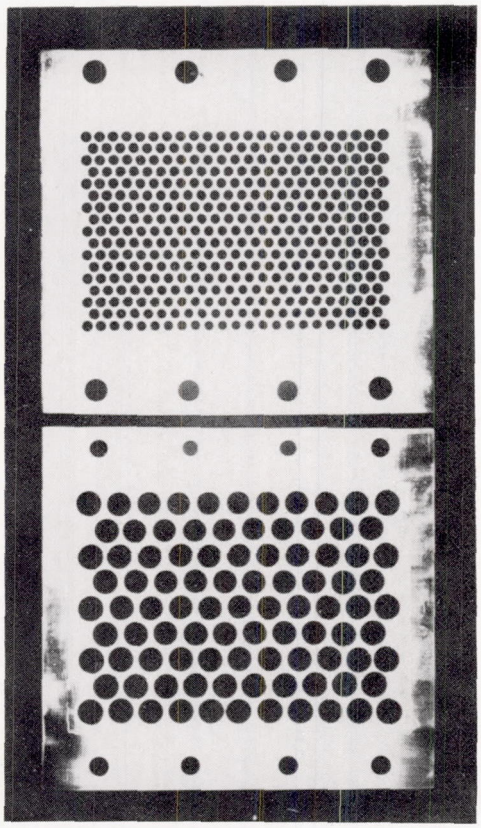

L-95825

(a) Diameter of holes, 0.25 inch; solidity ratios, 0.25.

(b) Diameter of holes, 0.512 inch; solidity ratios, 0.25.

Figure 5.- Grids used in investigation.

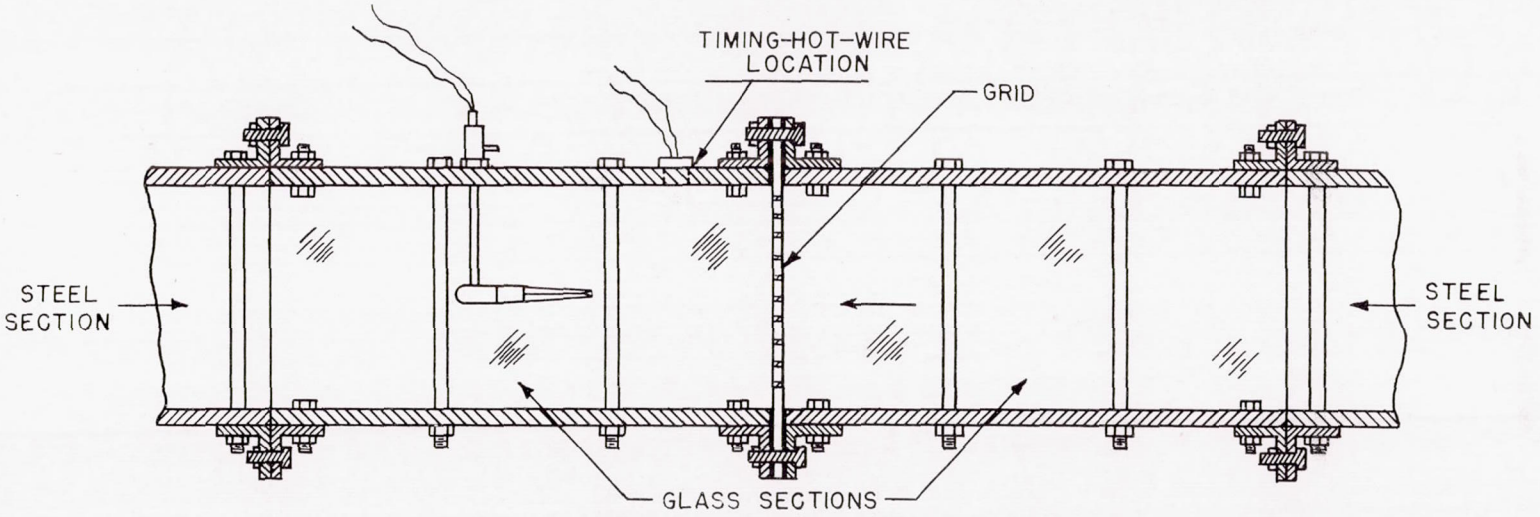

Figure 6.- Mounting of grid.

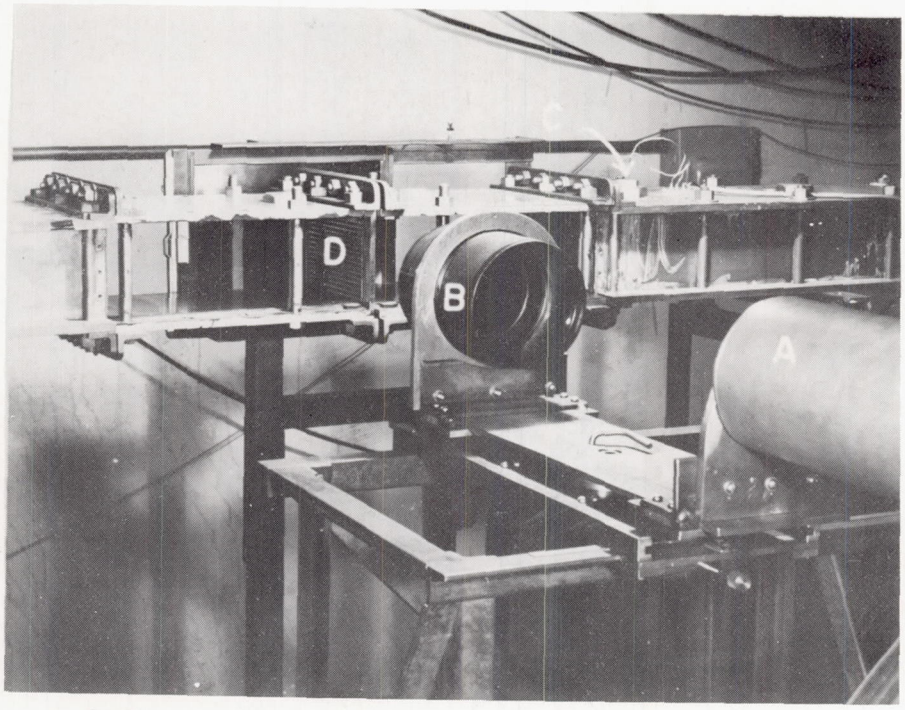

L-92438

Figure 7.- Working section and arrangement for taking shadowgraphs. A, spark point source of light; B, collimating lens; C, timing and triggering hot-wire; D, grid.

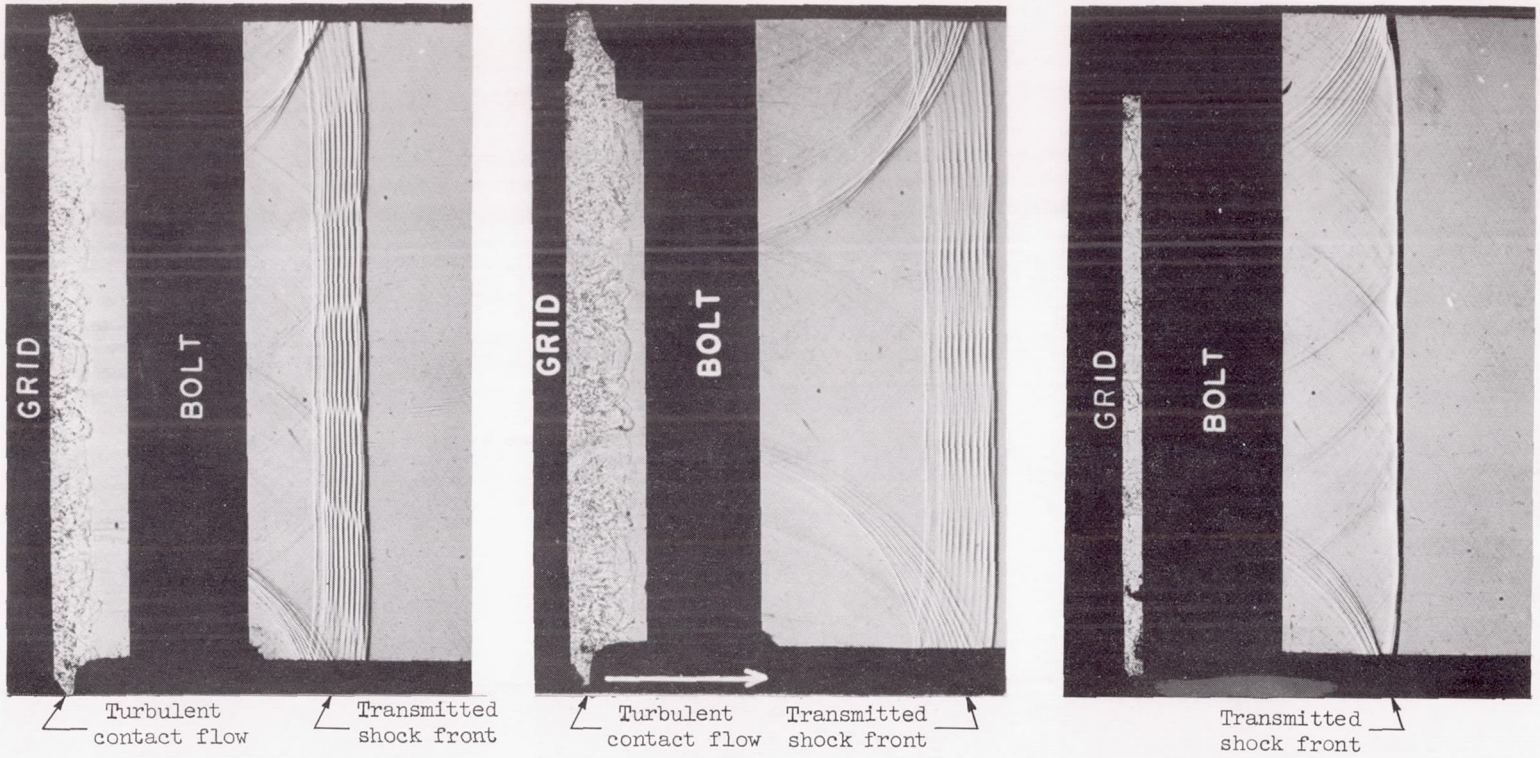

L-95826

(a) Transmitted shock; divergent beam of light with shock front about 4° off axis of beam. Delay, 120 microseconds; d, 0.512 inch.

(b) Transmitted shock; divergent beam of light with shock front about 5° off axis of beam. Delay, 150 microseconds; d, 0.512 inch.

(c) Transmitted shock; divergent beam of light with shock front in line with axis of beam. Delay, 120 microseconds; d, 0.512 inch.

Figure 8.- Shadowgraphs of transmitted and reflected shock through 25-percent-solidity grid. S = 1.58.

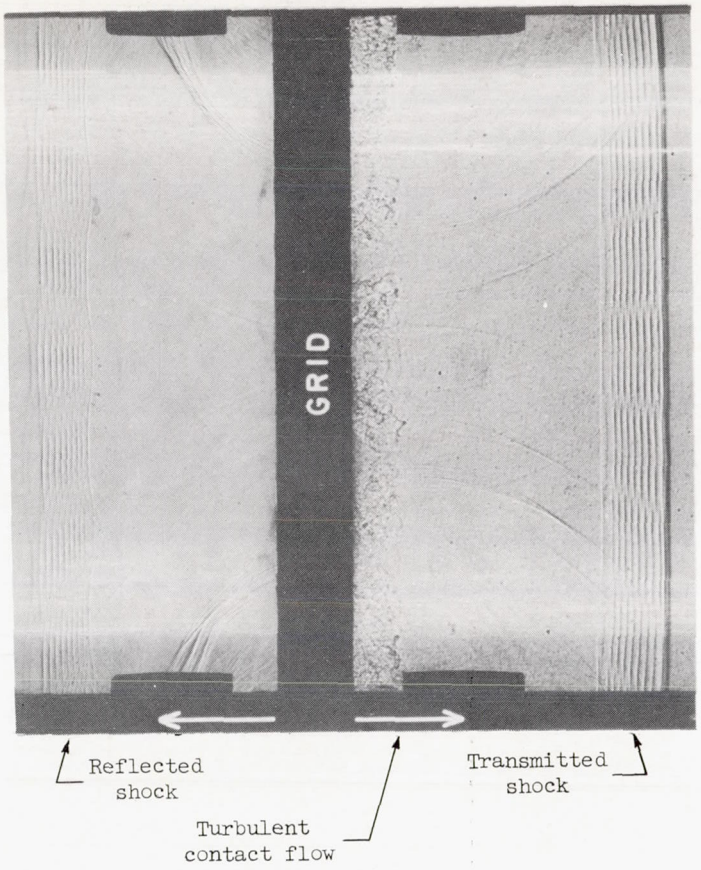

(d) Transmitted and reflected shock; grid mounted between two glass sections; divergent beam of light with shock fronts off axis of beam. Delay, 140 microseconds; d, 0.512 inch.

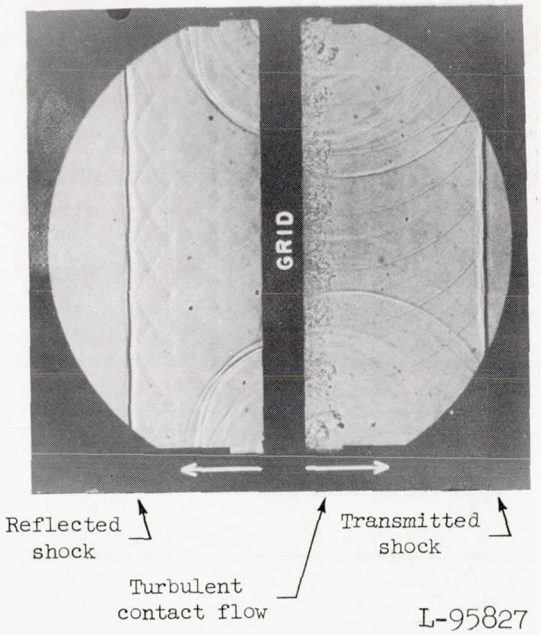

(e) Transmitted and reflected shock; grid mounted between two glass sections; collimated beam of light (field of view, 4.4 inches). Delay, 140 microseconds; d, 0.512 inch.

Figure 8.- Continued.

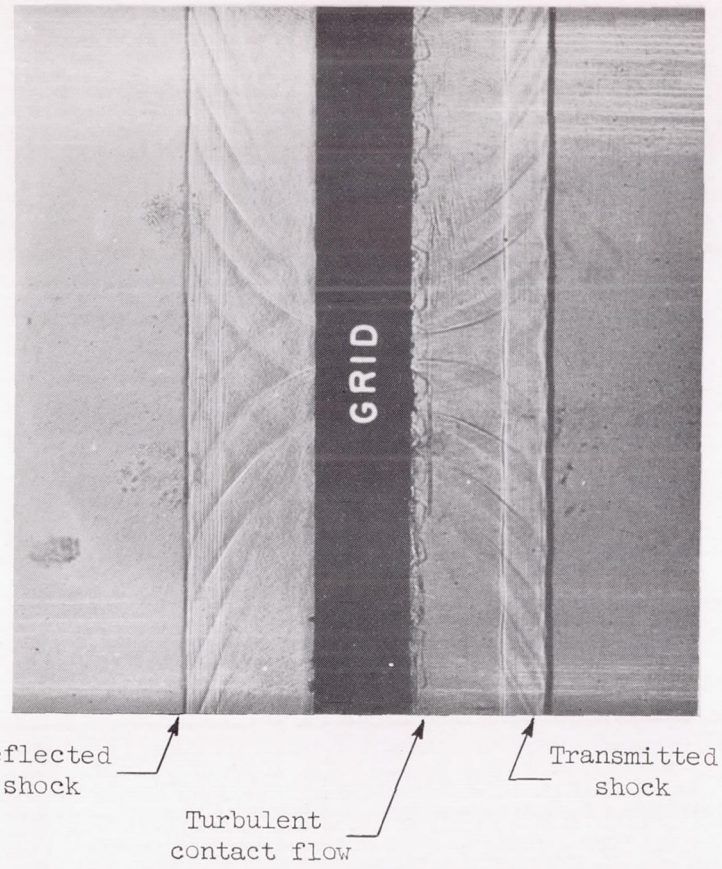

(f) Transmitted and reflected shock; grid mounted betweeen two glass sections; divergent beam of light with shock fronts off axis of beam. Delay, 60 microseconds; d, 0.25 inch; S_R = 1.11; S_T = 1.55.

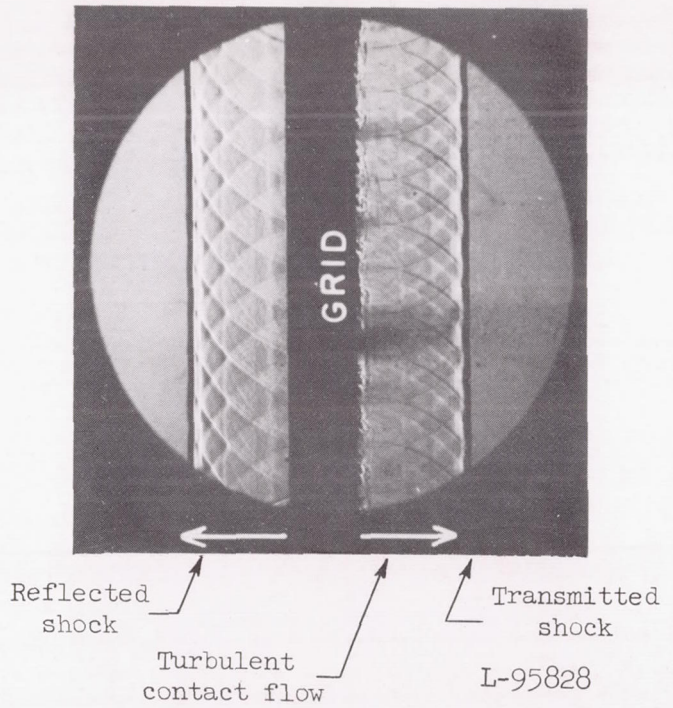

(g) Transmitted and reflected shock; grid mounted between two glass sections; collimated beam of light (field of view, 2.6 inches). Note refraction waves following shock waves. Delay, 60 microseconds; d, 0.25 inch; S_R = 1.11; S_T = 1.55.

Figure 8.- Concluded.

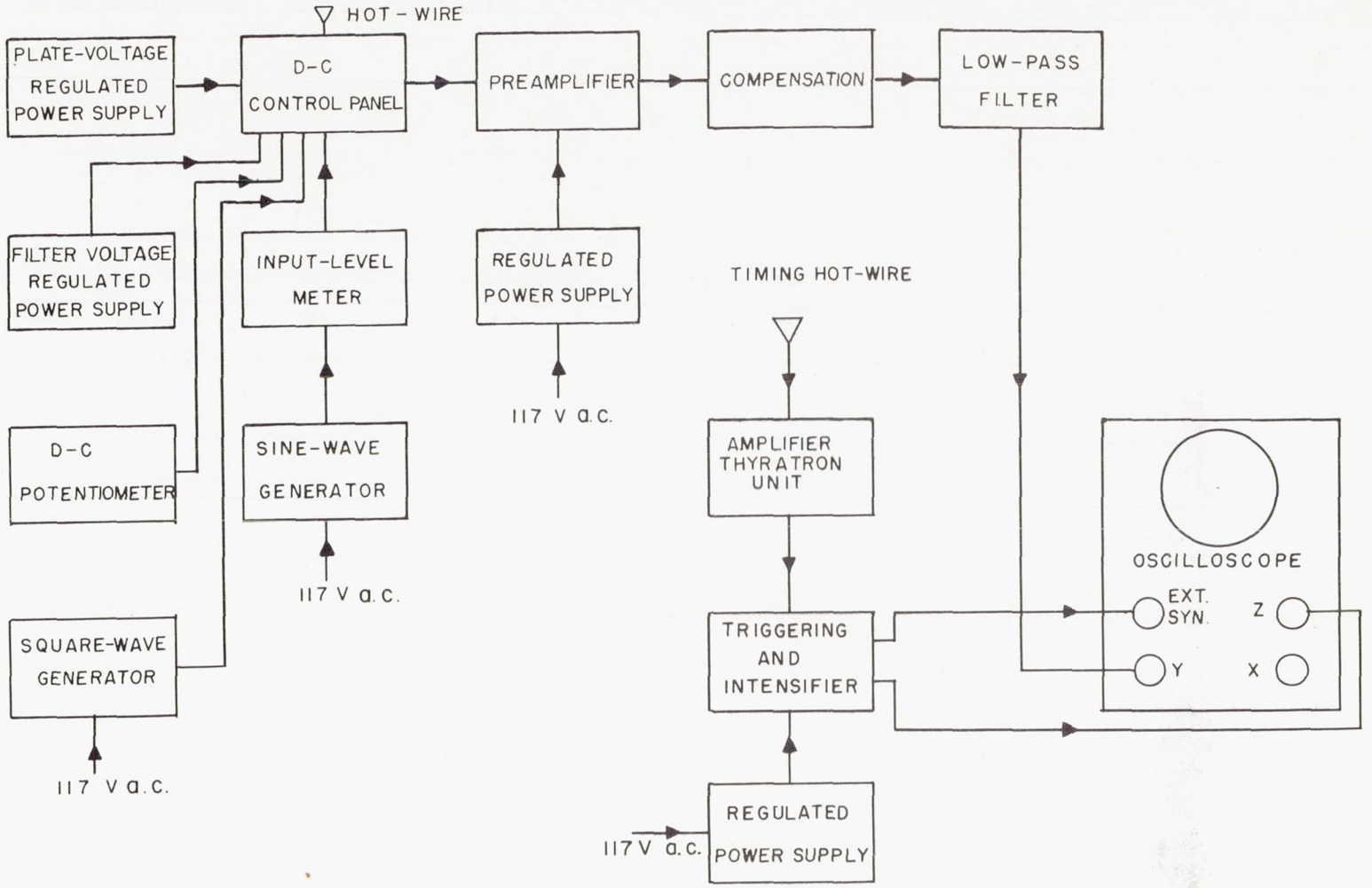

Figure 9.- Block diagram of hot-wire equipment.

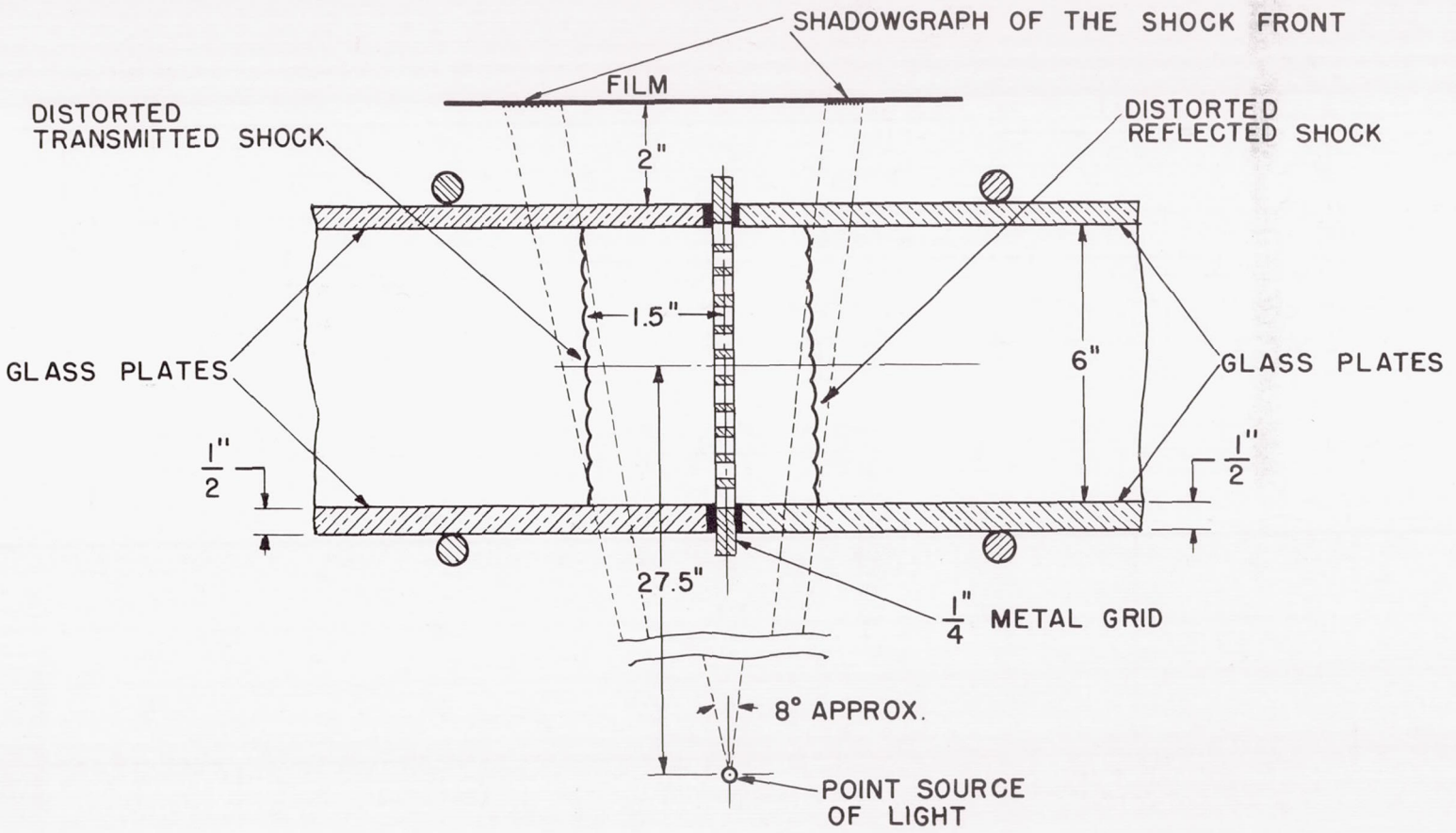

Figure 10.- Light arrangement for shadowgraphs taken from rear of shock front. Distances for light source are approximate.

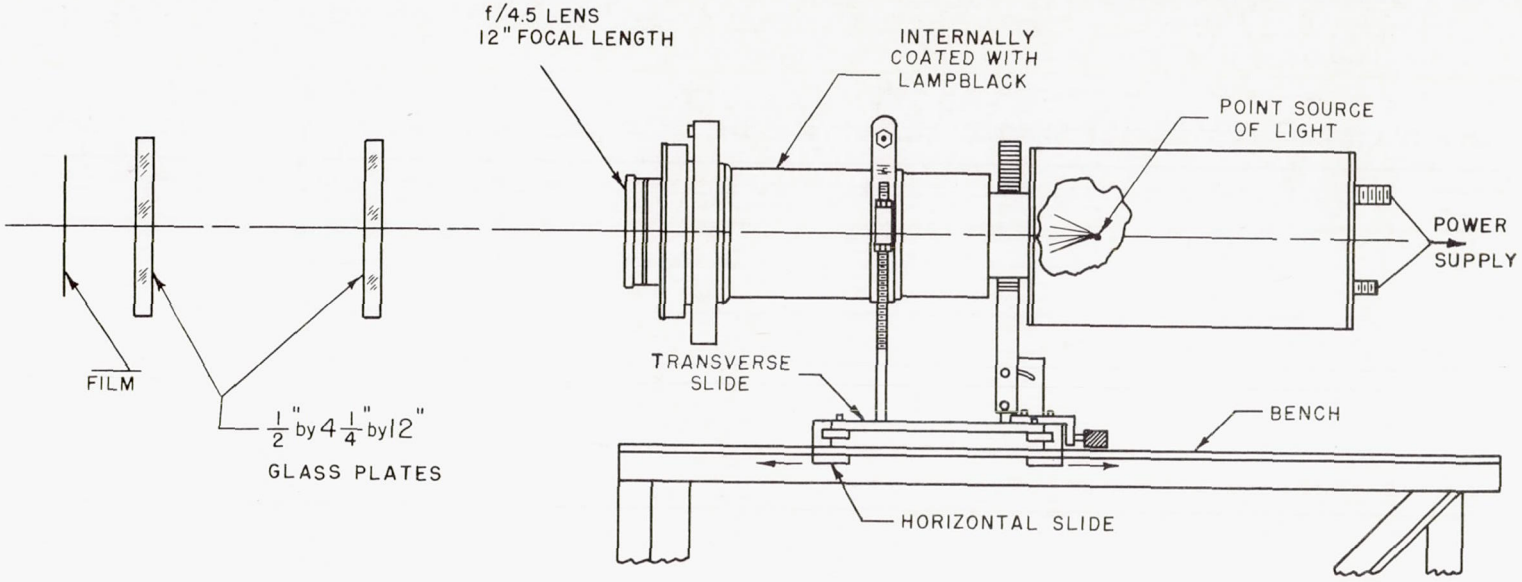

Figure 11.- Arrangement for shadowgraphs.

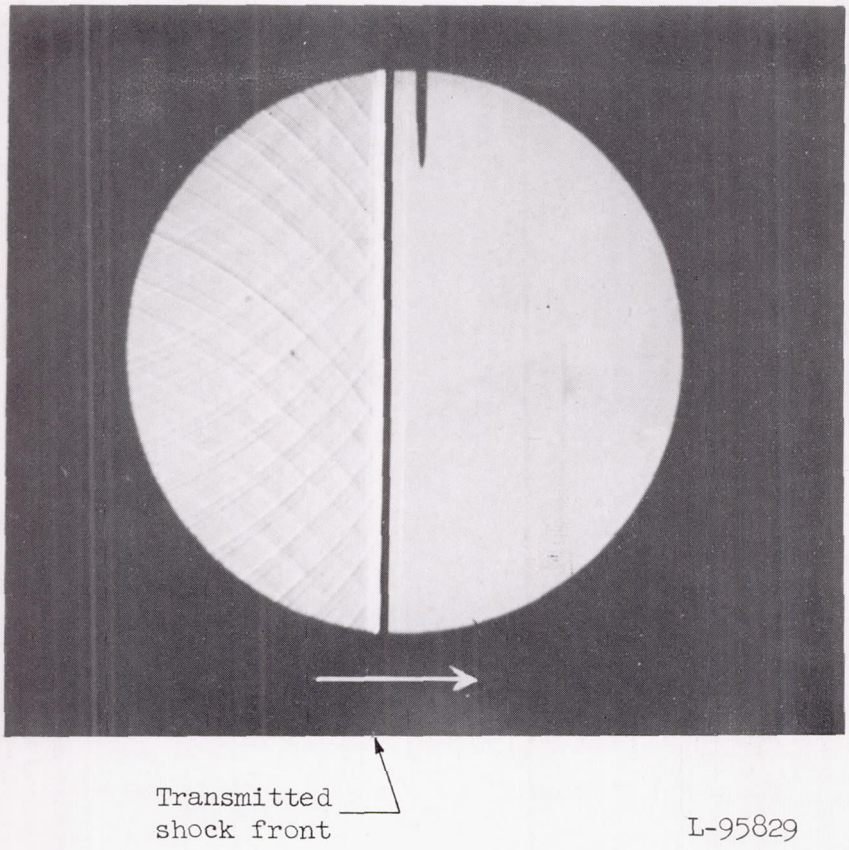

(a) Transmitted shock; collimated beam of light (field of view, 2.6 inches); shock front located 3 inches downstream from grid; delay, 200 microseconds. $S = 1.58$; $S_T = 1.55$; $d = 0.25$ inch.

Figure 12.- Interaction of reflected transmitted shock with turbulent contact flow through 25-percent-solidity grid.

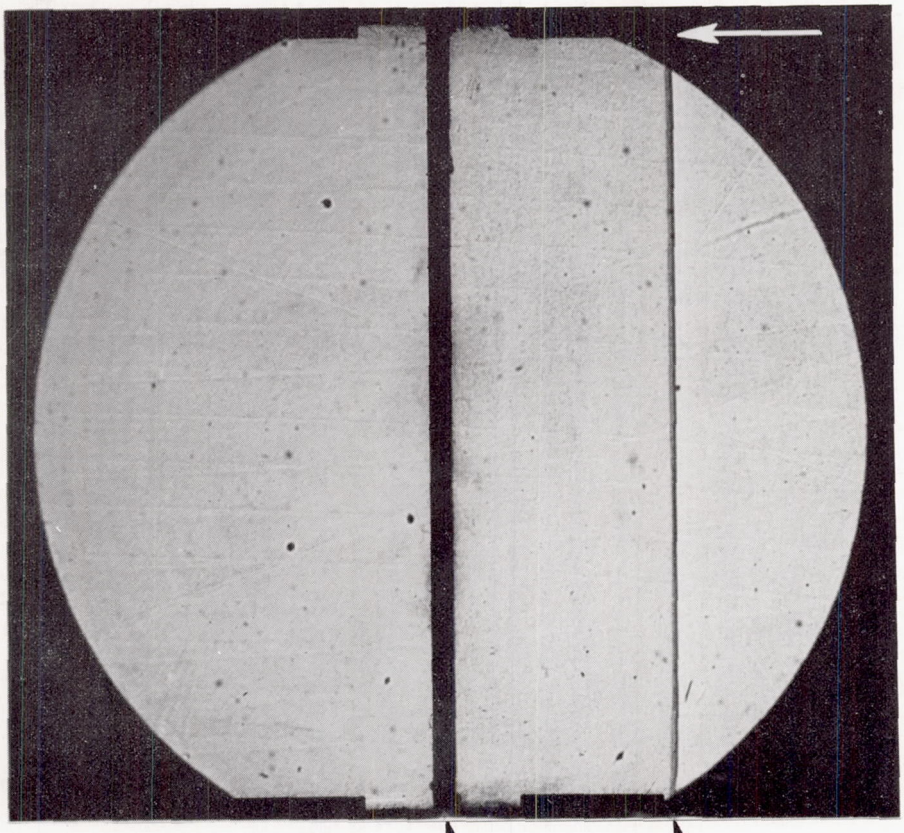

(b) Reflected transmitted shock; collimated beam of light (field of view, 4.4 inches); shock front located $13\frac{9}{32}$ inches downstream from grid; delay, 2,320 microseconds; closed end $24\frac{3}{8}$ inches downstream from grid. $S = 1.58$; $S_T = 1.55$; $S_T' \approx 1.51$; $d = 0.25$ inch.

Figure 12.- Continued.

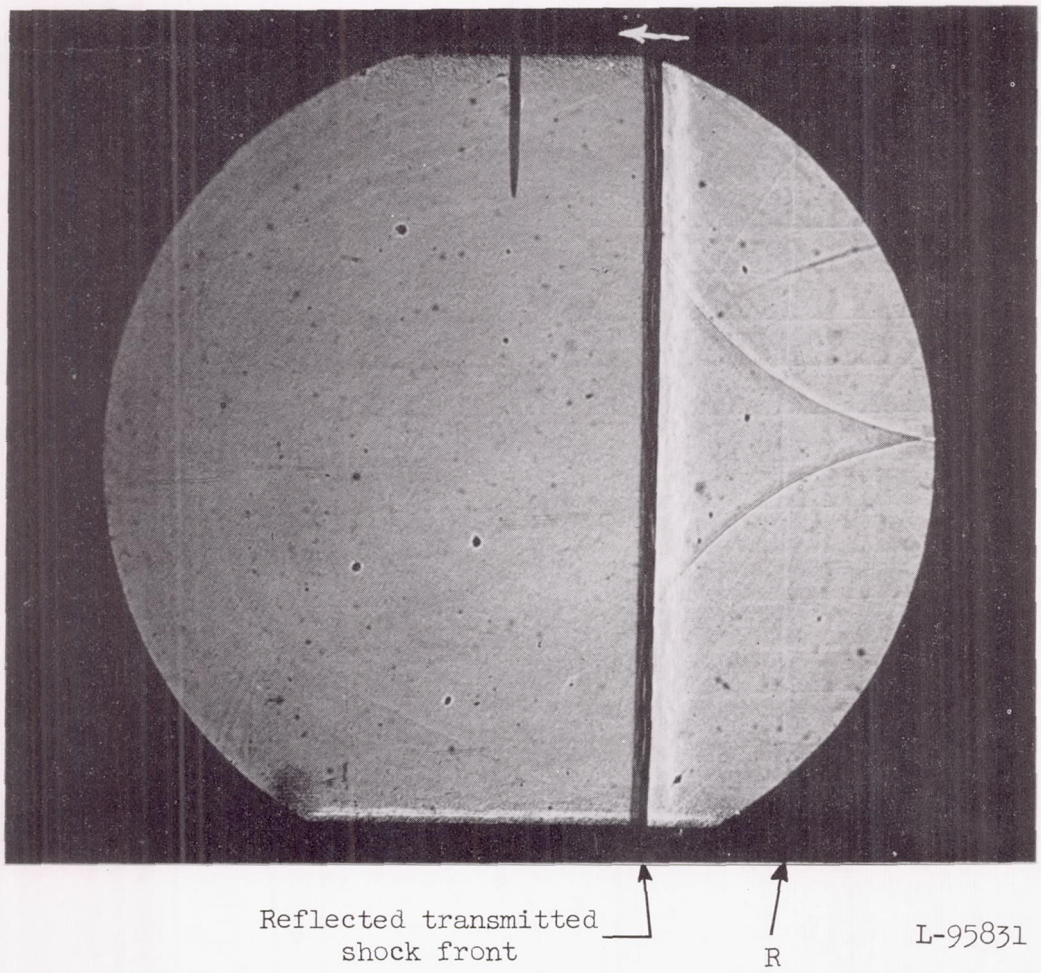

(c) Reflected transmitted shock; collimated beam of light (field of view, 4.4 inches); shock front located $10\frac{1}{4}$ inches downstream from grid; delay 2,531 microseconds; closed end 2 feet downstream from grid. $S = 1.58$; $S_T = 1.55$; $S_T' \approx 1.51$; $d = 0.25$ inch. At back of and parallel to shock front and weak wave front R was observed and possibility of its being a rarefaction wave front is not ruled out.

Figure 12.- Continued.

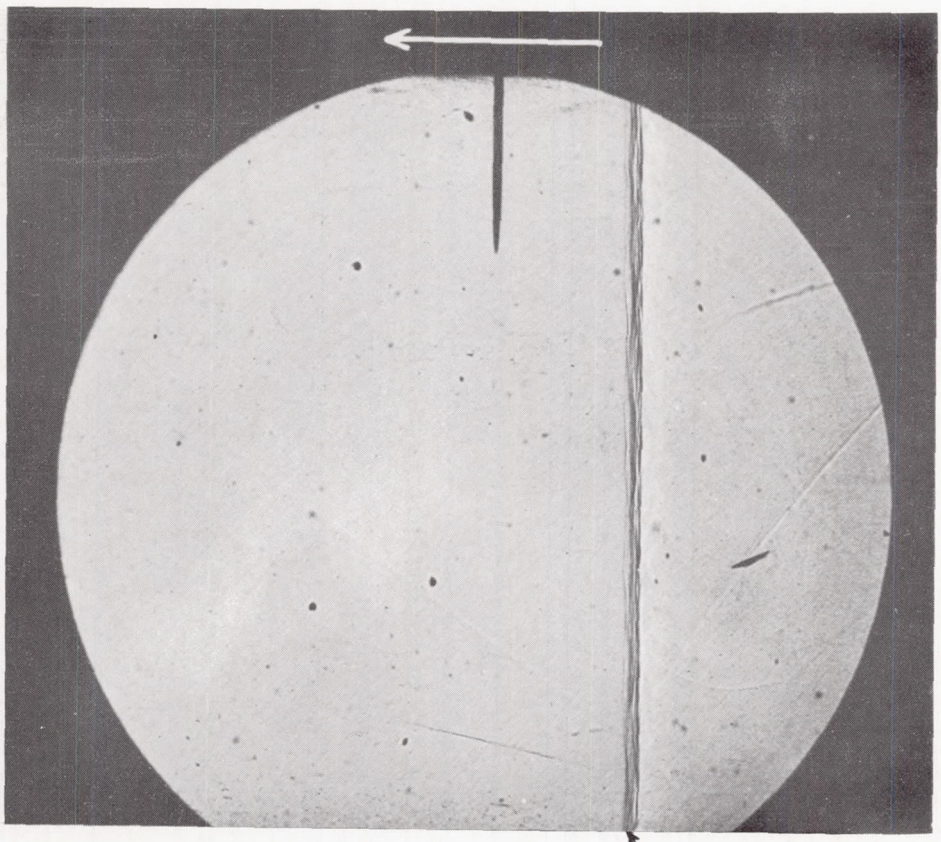

(d) Reflected transmitted shock; collimated beam of light (field of view, 4.4 inches); shock front located $4\frac{1}{4}$ inches downstream from grid; delay, 3,010 microseconds; closed end 2 feet downstream from grid. $S = 1.58$; $S_T = 1.55$; $S_T' \approx 1.51$; $d = 0.25$ inch.

Figure 12.- Continued.

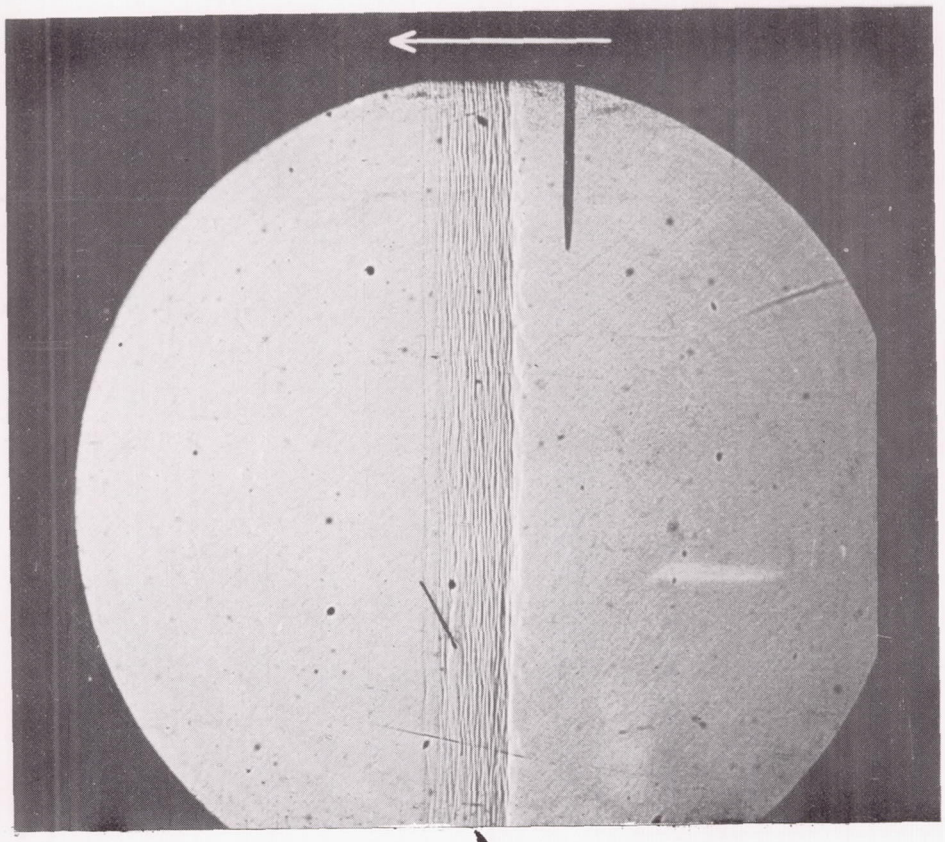

(e) Reflected transmitted shock; collimated beam of light inclined at 4° angle with respect to shock front (field of view, 4.4 inches); shock front located approximately $3\frac{1}{4}$ inches downstream from grid; delay, 3,080 microseconds; closed end 2 feet downstream from grid. $S = 1.58$; $S_T = 1.55$; $S_T' \approx 1.51$; $d = 0.25$ inch.

Figure 12.- Continued.

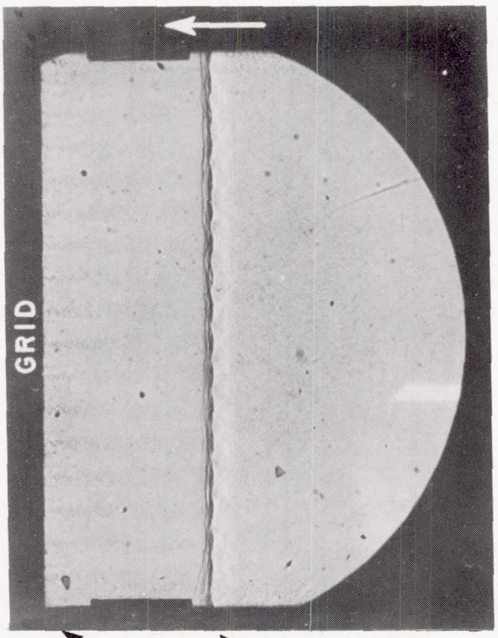

(f) Reflected transmitted shock and turbulent contact flow (jets); collimated beam of light (field of view, 4.4 inches); shock front located $1\frac{3}{8}$ inches downstream from grid; delay, 3,230 microseconds; closed end 2 feet downstream from grid. $S = 1.58$; $S_T = 1.55$; $S_T' \approx 1.51$; $d = 0.25$ inch.

Figure 12.- Continued.

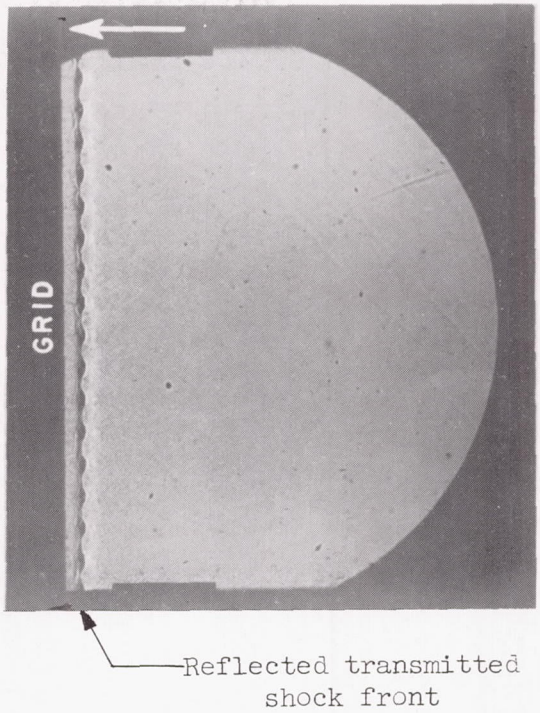

(g) Reflected transmitted shock; collimated beam of light (field of view, 4.4 inches); shock front located 1/4 inch downstream from grid; delay, 3,340 microseconds; closed end 2 feet downstream from grid. $S = 1.58$; $S_T = 1.55$; $S_T' \approx 1.51$; $d = 0.25$ inch.

Figure 12.- Continued.

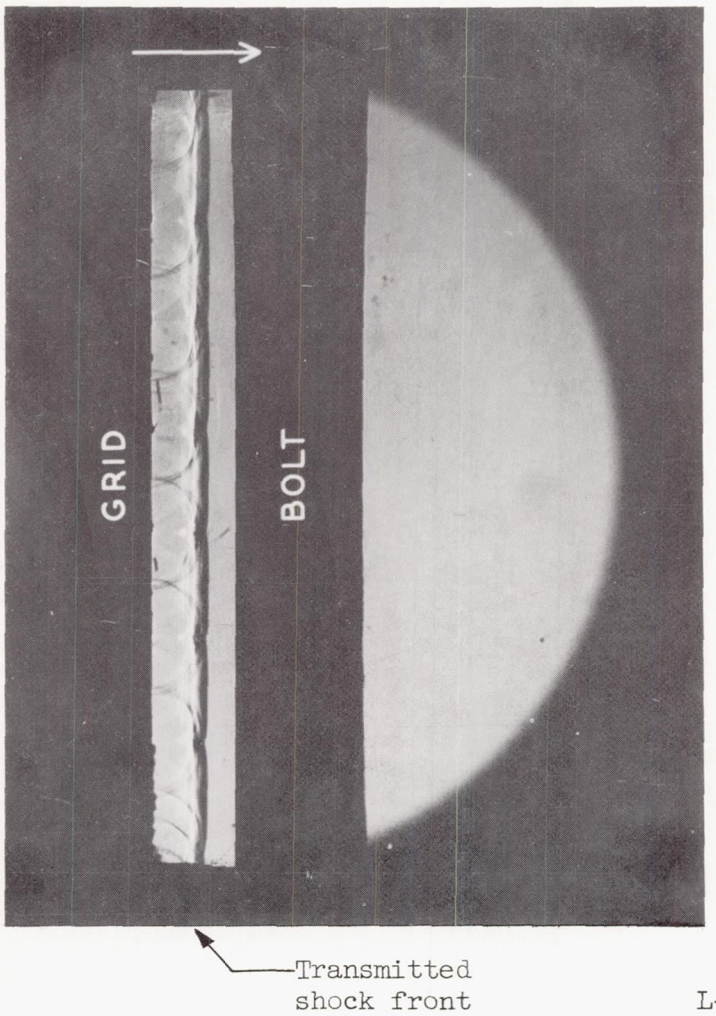

(h) Transmitted shock; divergent beam of light with shock front in line with axis of beam; delay, 27 microseconds; closed end 12 inches downstream from grid. S = 1.387; d = 0.512 inch.

Figure 12.- Continued.

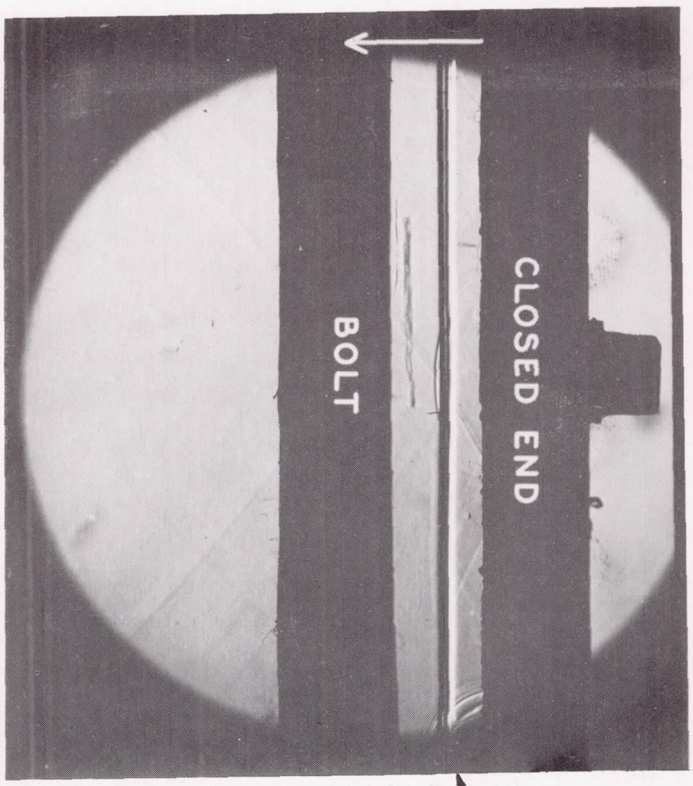

(i) Reflected transmitted shock; collimated beam of light (field of view, 4.4 inches); delay, 816 microseconds; closed end 12 inches downstream from grid. S = 1.387; d = 0.512 inch.

Figure 12.- Continued.

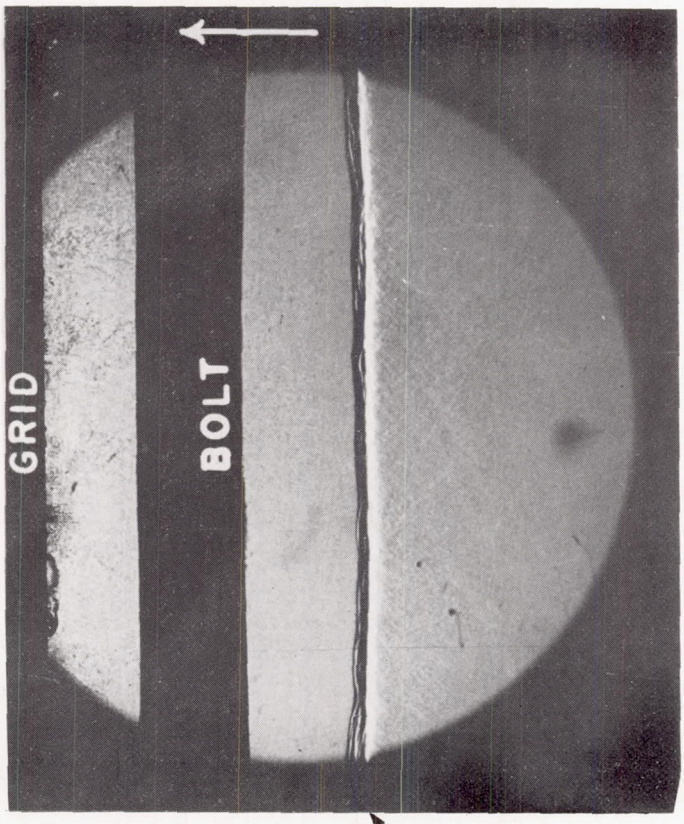

(j) Reflected transmitted shock; collimated beam of light (field of view, 4.4 inches); delay, 1,581 microseconds; closed end 12 inches downstream from grid. S = 1.387; d = 0.512 inch.

Figure 12.- Continued.

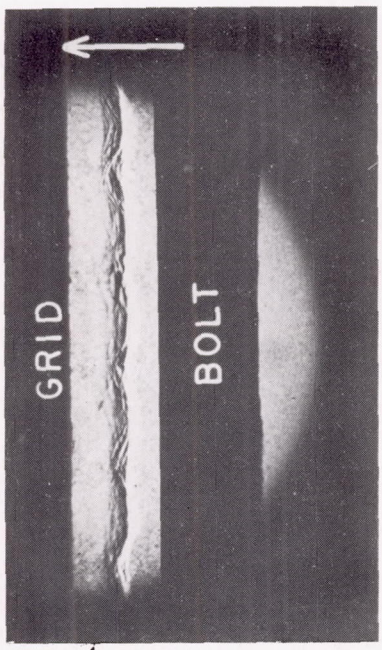

(k) Reflected transmitted shock; collimated beam of light (field of view, 2.6 inches); delay, 1,676 microseconds; closed end 12 inches downstream from grid. S = 1.387; d = 0.512 inch.

Figure 12.- Continued.

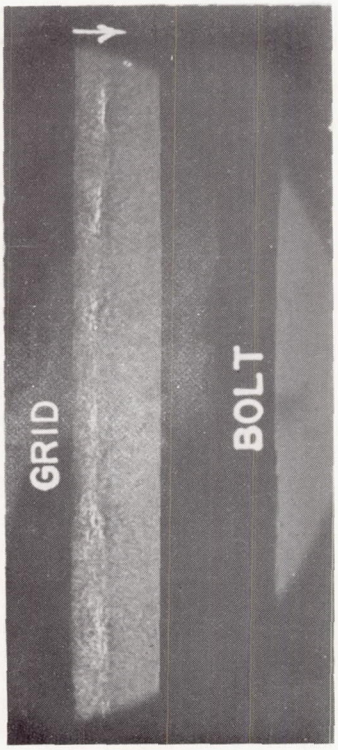

L-95840

(l) Reflected transmitted shock again reflected from grid; collimated beam of light (field of view, 4.4 inches); delay, 1,716 microseconds; closed end 12 inches downstream from grid. S = 1.387; d = 0.512 inch.

Figure 12.- Continued.

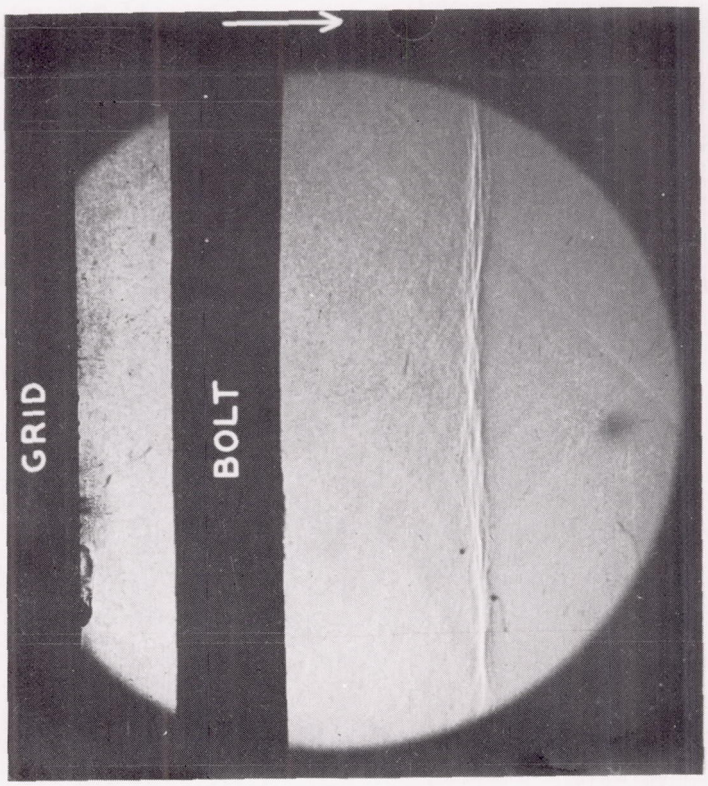

L-95841

(m) Reflected transmitted shock again reflected from grid; collimated beam of light (field of view, 4.4 inches); delay, 1,916 microseconds; closed end 12 inches downstream from grid. S = 1.387; d = 0.512 inch.

Figure 12.- Continued.

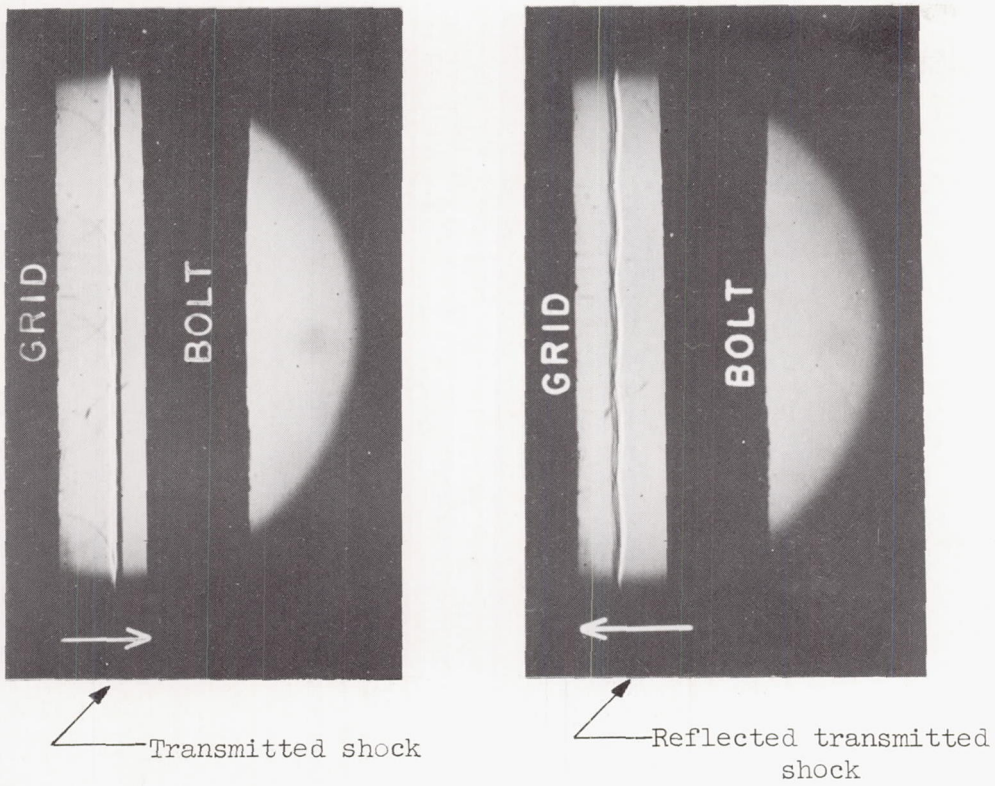

L-95842

(n) Transmitted shock; collimated beam of light (field of view, 2.6 inches); delay, 30 microseconds; closed end 12 inches downstream from grid. S = 1.09; d = 0.512 inch.

(o) Reflected transmitted shock; collimated beam of light (field of view, 2.6 inches); delay, 1,790 microseconds; closed end 12 inches downstream from grid. S = 1.09; d = 0.512 inch.

Figure 12.- Concluded.

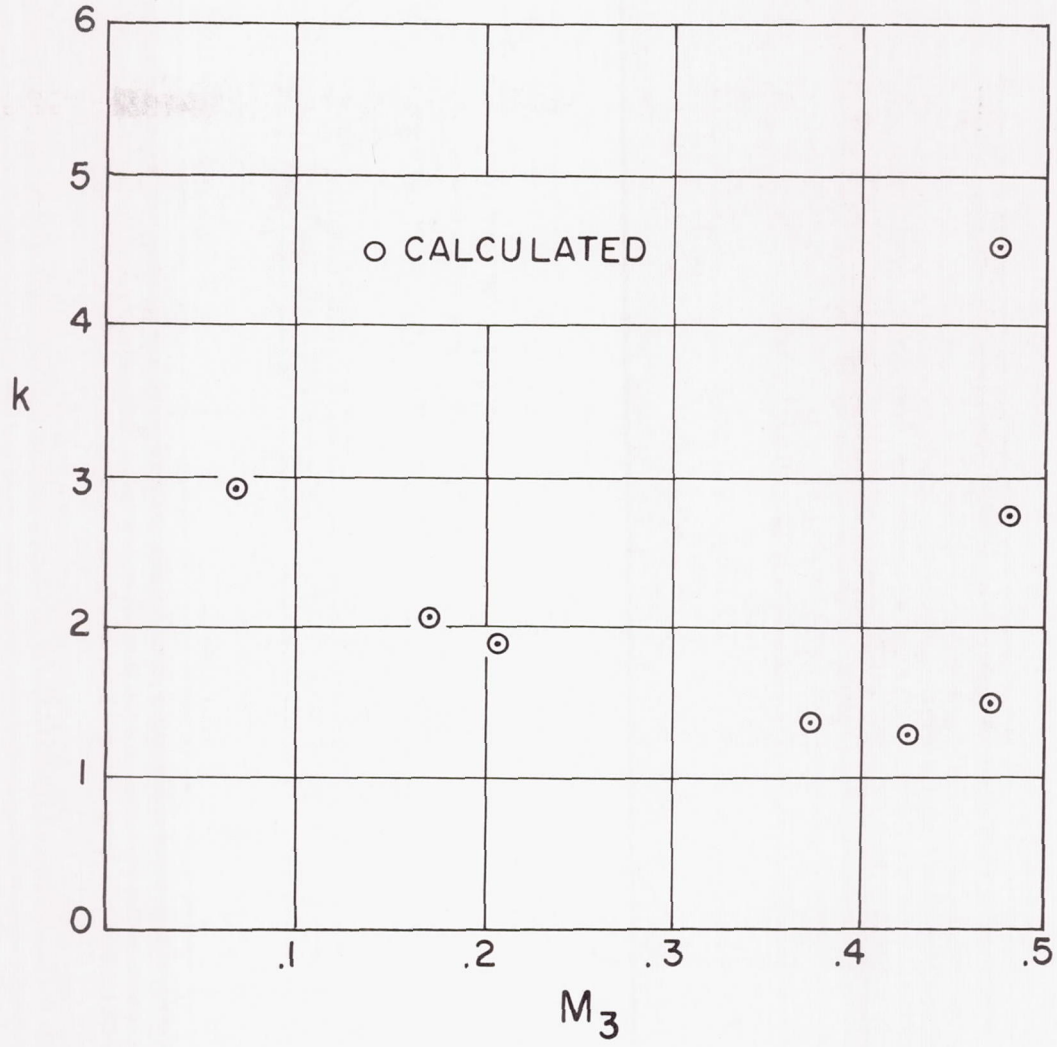

Figure 13.- Mach number M_3 versus pressure-drop coefficient k.

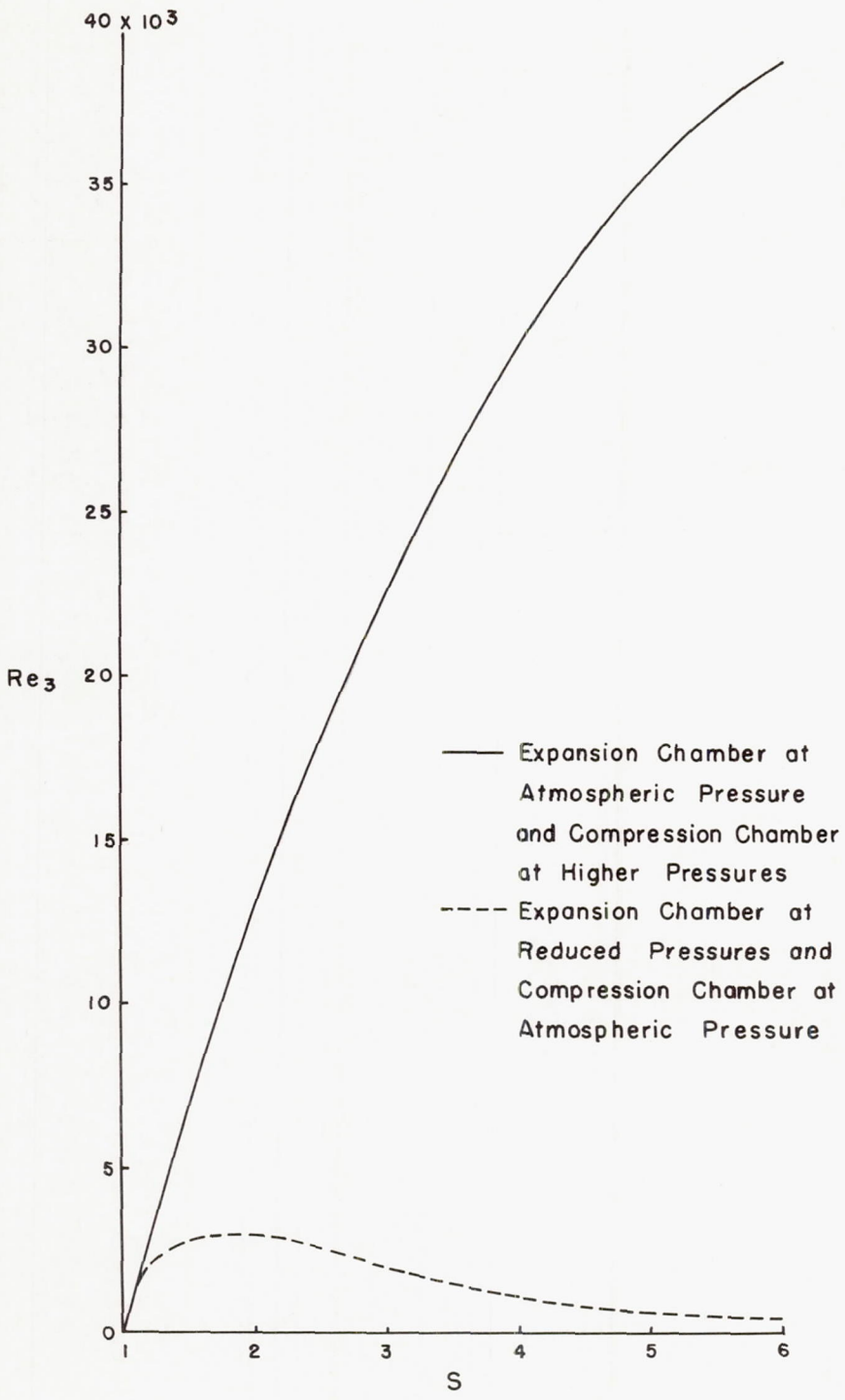

Figure 14.- Reynolds number versus shock strength. $Re_3 = \frac{\rho_3 u_3 b_{eff}}{\mu_3}$.

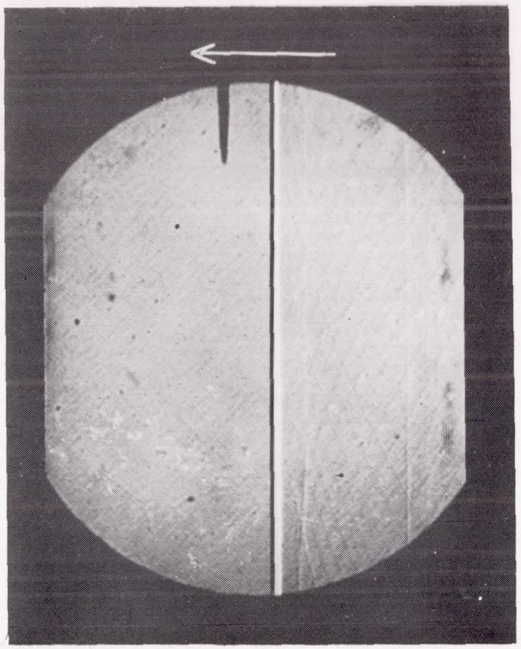

(a) Collimated beam of light (field of view, 2.6 inches); shock front located $9\frac{3}{4}$ inches upstream from grid; delay, 1,580 microseconds. $S = 1.387$; $S_R = 1.081$; $S_T = 1.373$.

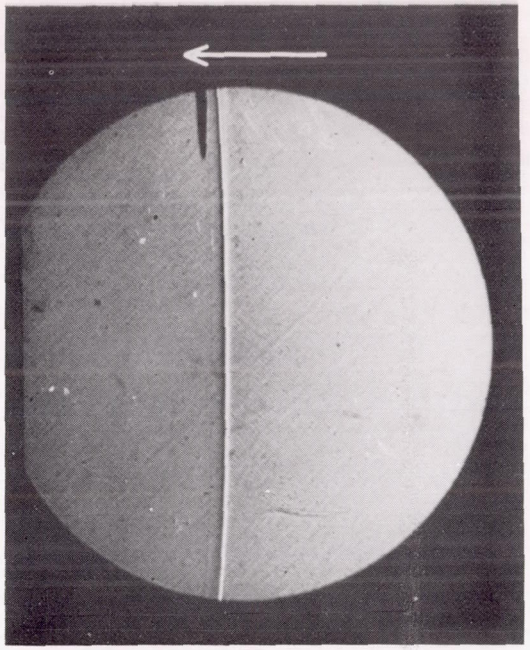

L-95843

(b) Collimated beam of light (field of view, 2.6 inches); shock front located $9\frac{29}{32}$ inches upstream from grid; delay, 1,780 microseconds. $S = 1.98$; $S_R = 1.139$; $S_T = 1.957$.

Figure 15.- Appearance of curvature in shock front reflected from grid with 0.25-inch-diameter holes.

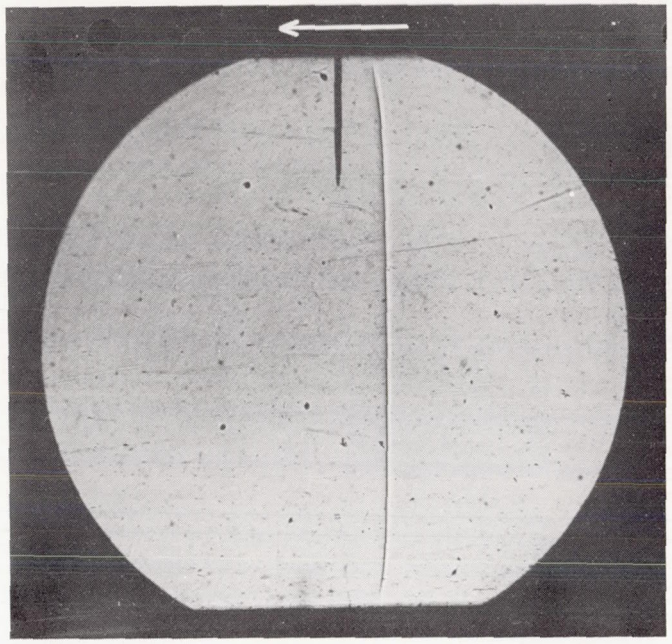

(c) Collimated beam of light (field of view, 4.4 inches); shock front located $3\frac{1}{4}$ inches upstream from grid; delay, 430 microseconds. S = 3.2; S_R = 1.461; S_T = 3.05.

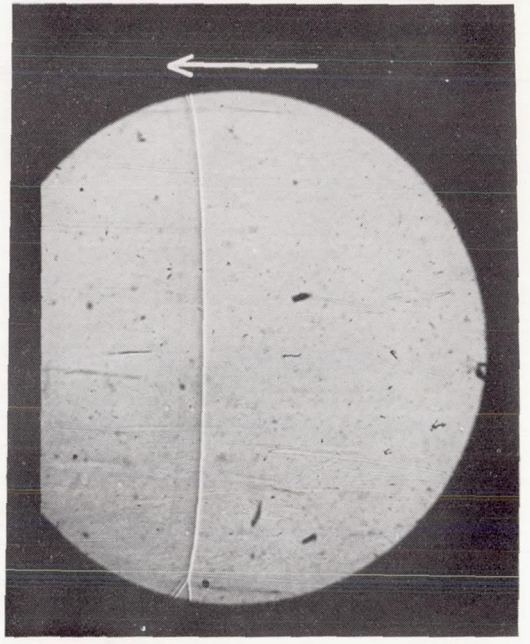

L-95844

(d) Collimated beam of light (field of view, 2.6 inches); shock front located 2 inches upstream from grid; delay, 780 microseconds. S = 5.68; S_R = 2.095; S_T = 5.163.

Figure 15.- Continued.

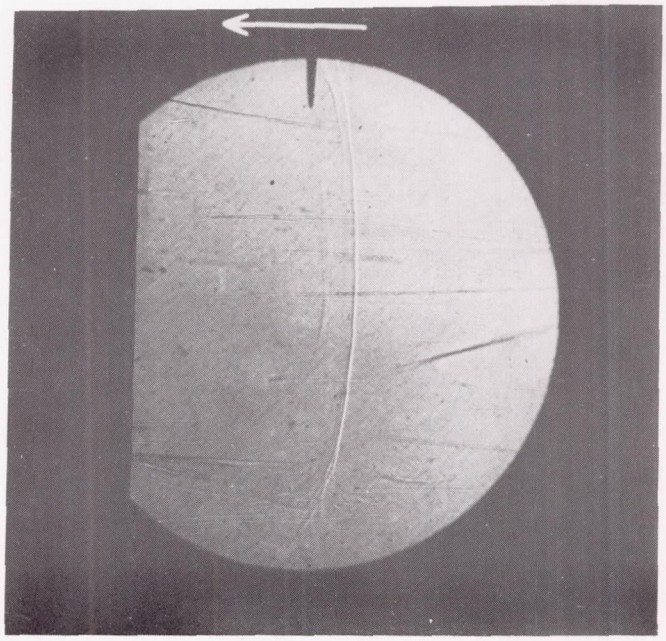

L-95845

(e) Collimated beam of light (field of view, 2.6 inches); shock front located $9\frac{3}{4}$ inches upstream from grid; delay, 2,100 microseconds. $S = 5.68$; $S_R = 2.095$; $S_T = 5.163$.

Figure 15.- Concluded.

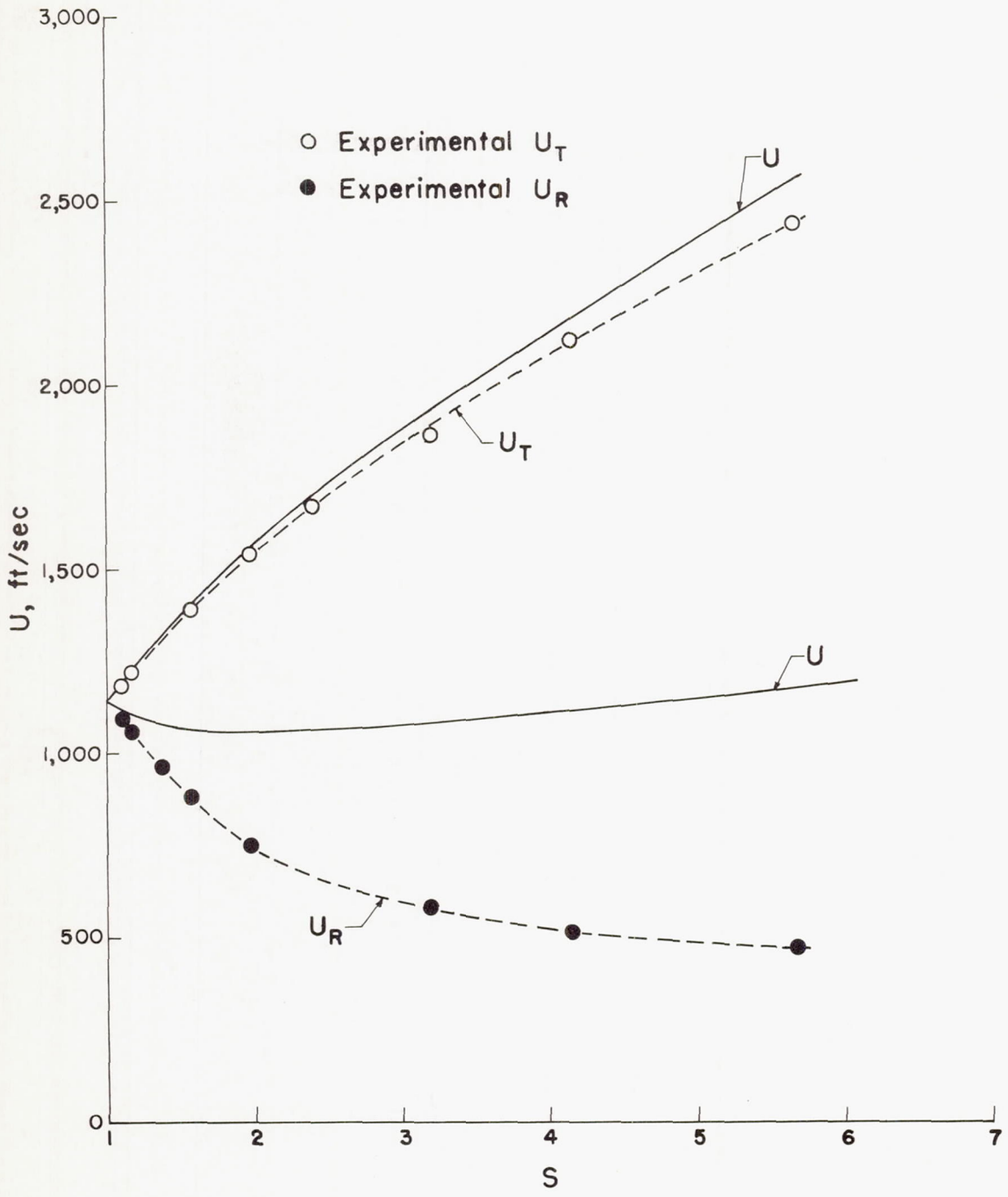

Figure 16.- Shock velocities versus incident shock strength.

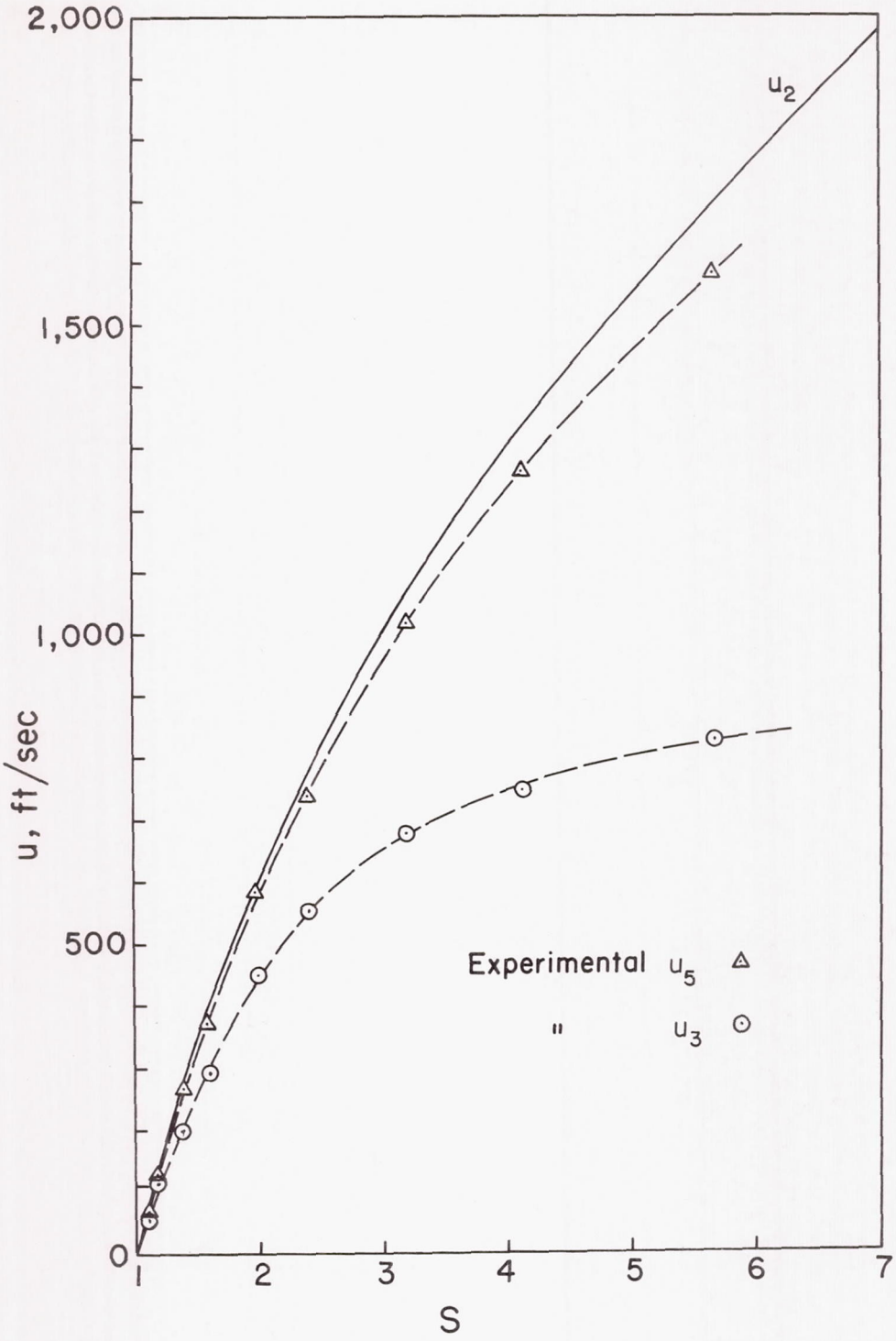

Figure 17.- Drift velocities versus incident shock strength.

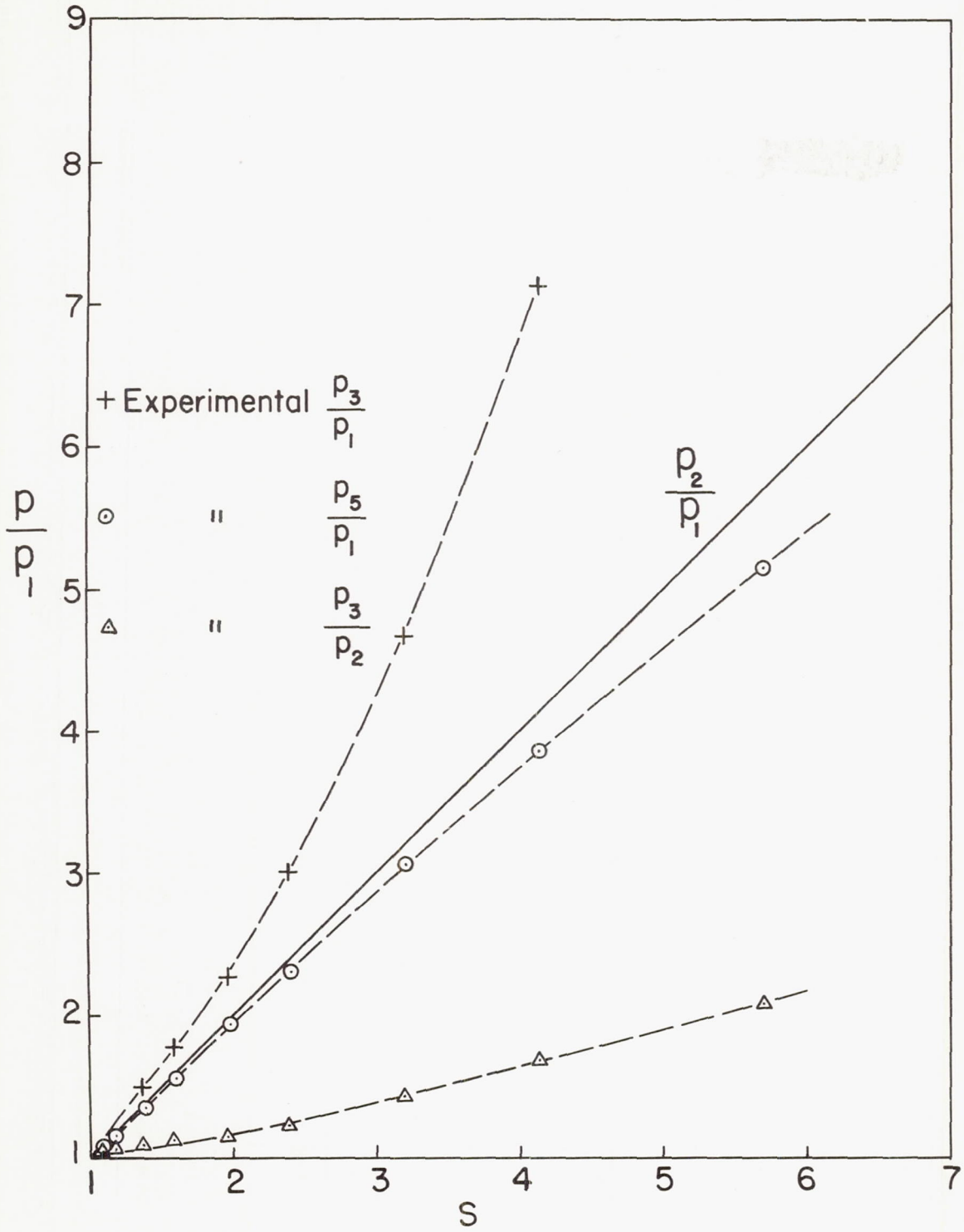

Figure 18.- Pressure ratios versus incident shock strength.

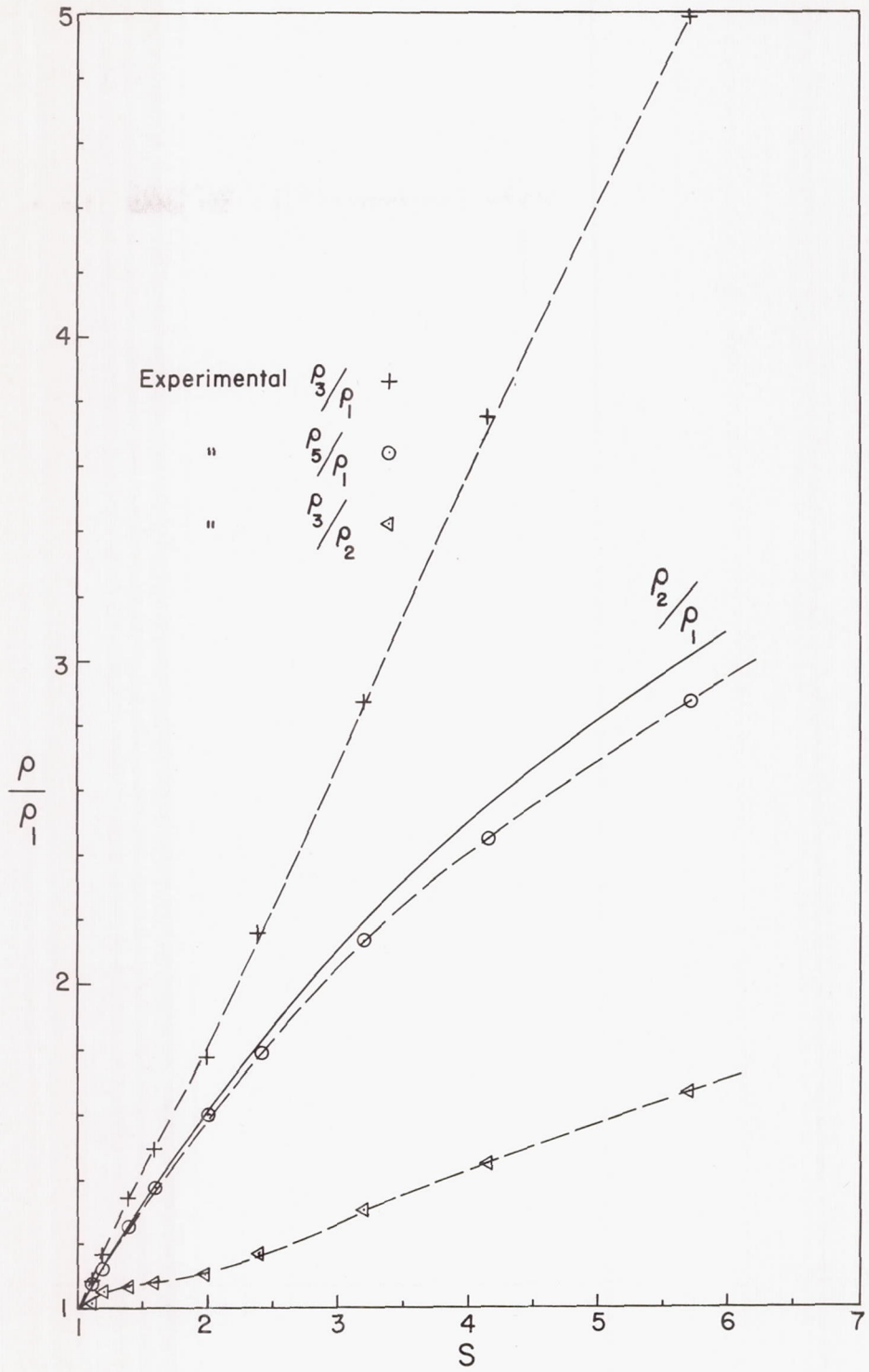

Figure 19.- Density ratios versus incident shock strength.

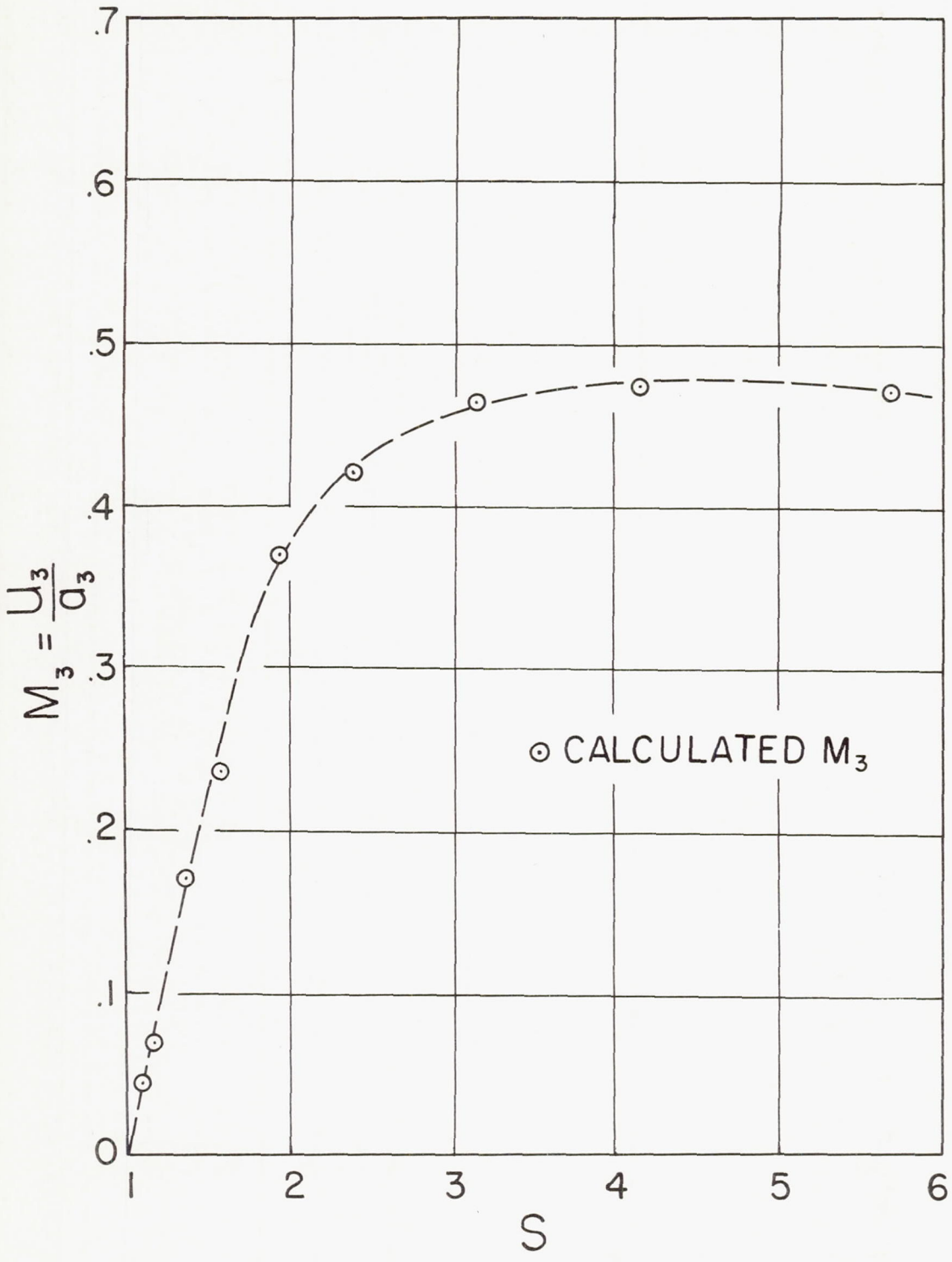

Figure 20.- Mach number M_3 versus incident shock strength.

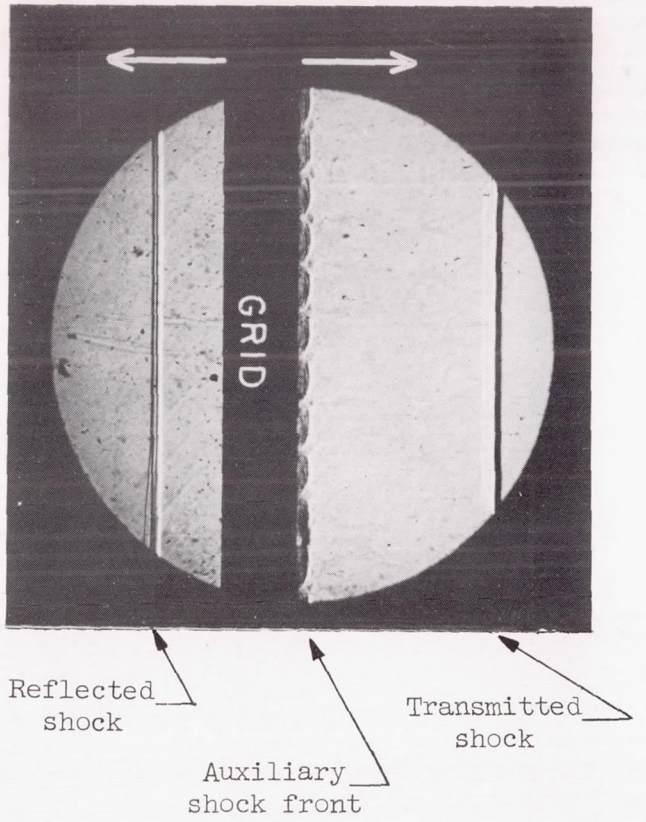

(a) Collimated beam of light (field of view, 2.6 inches). Delay, 65 microseconds.

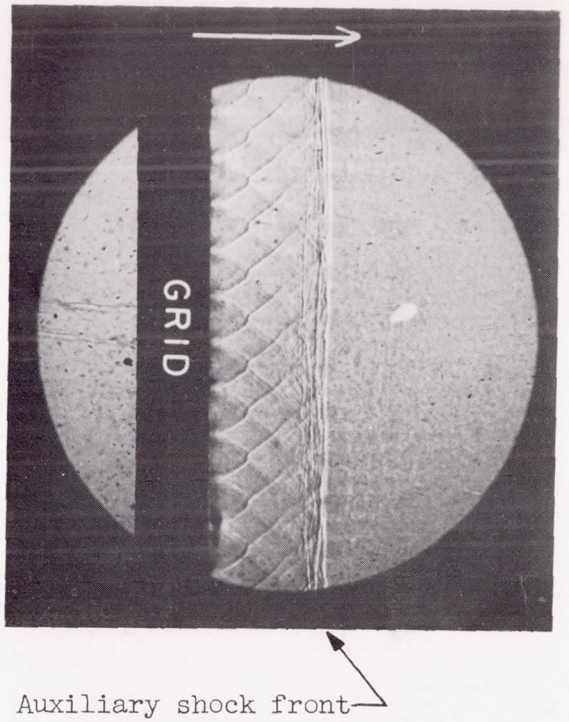

L-95846

(b) Collimated beam of light (field of view, 2.6 inches). Delay, 1,370 microseconds.

Figure 21.- Emergence of an auxiliary shock front through a 25-percent-solidity grid with 0.25-inch-diameter holes. $S = 3.2$; $S_T = 3.05$.

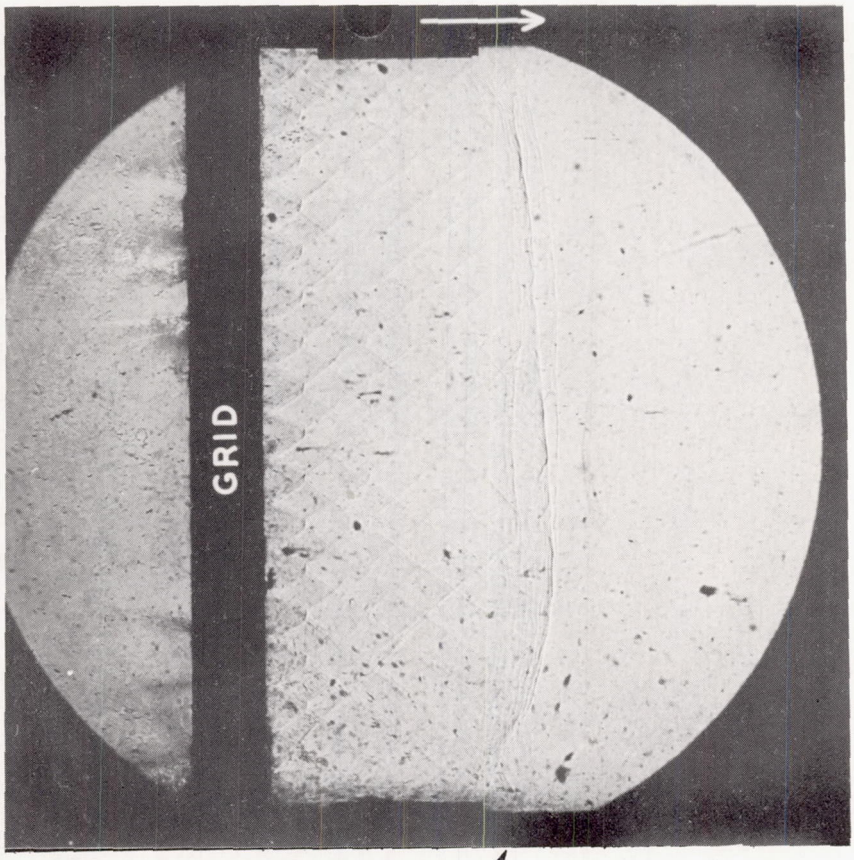

(c) Collimated beam of light (field of view, 4.4 inches). Delay, 4,330 microseconds.

Figure 21.- Concluded.

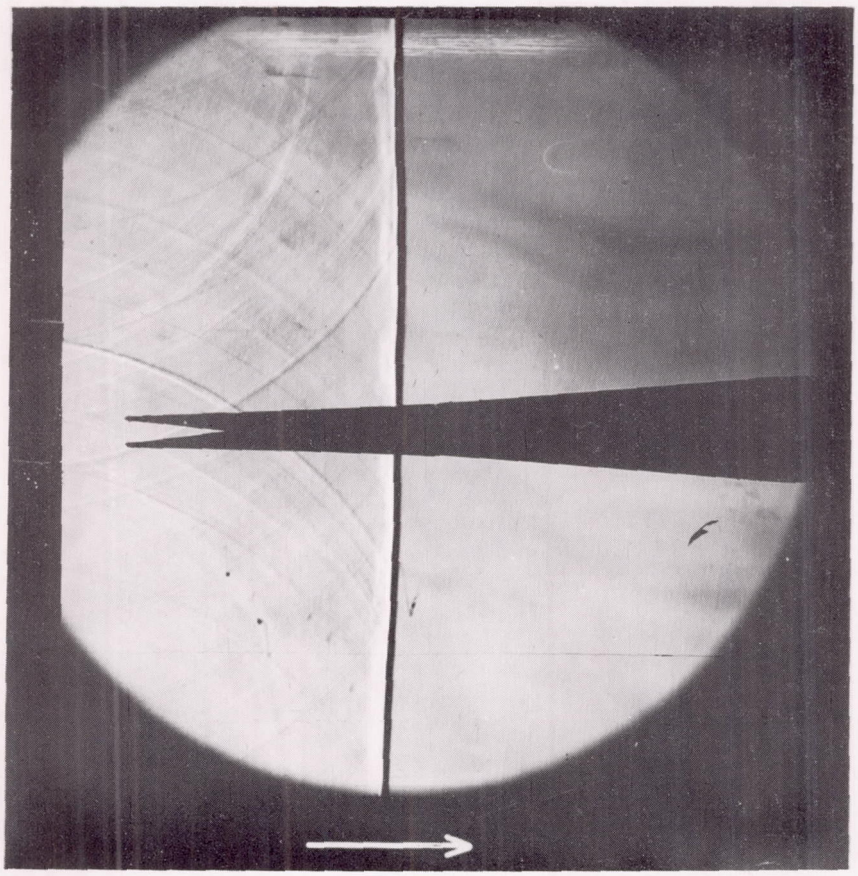

L-95848

Figure 22.- Passage of a transmitted shock wave over hot-wire probe.

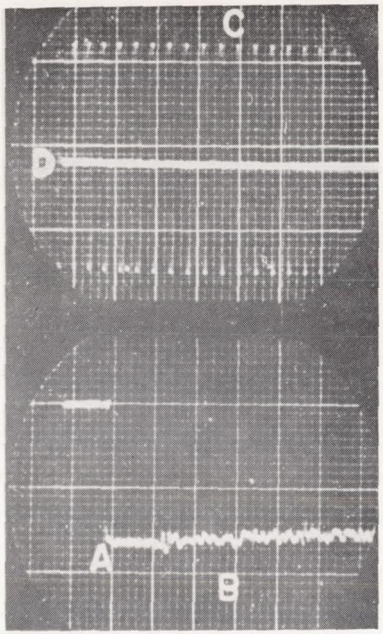

(a) Mass-flow response. Current, 27.74 milliamperes; resistance of wire with no current through it, 10.39 ohms; operating resistance, 15.52 ohms; compensation, 0.175×10^{-3} second; calibration signal, 45 millivolts root mean square at 10 kilocycles.

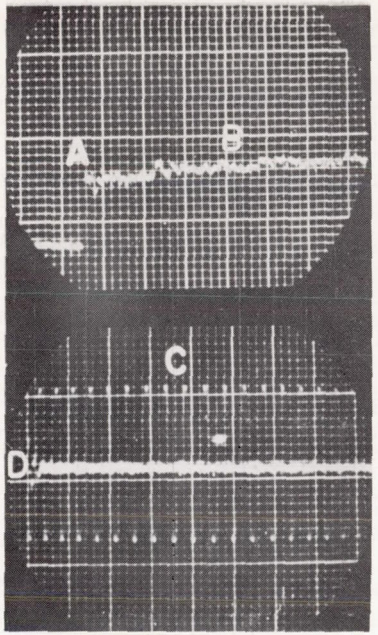

(b) Temperature response. Current, 2 milliamperes; operating resistance, 9.94 ohms; compensation, 0.17×10^{-3} second; calibration signal, 1.8 millivolts root mean square at 10 kilocycles.

Figure 23.- Mass-flow and temperature response to traveling transmitted shock. S = 1.58; S_T = 1.55. A, jump due to transmitted shock; B, contact surface flow; C, calibration signal; D, base trace for noise calibration. Location of hot-wire, $1\frac{9}{16}$ inches downstream from grid.